

UNIVERZITA PALACKÉHO OLMOUC
PŘÍRODOVĚDECKÁ FAKULTA
KATEDRA OPTIKY

DIPLOMOVÁ PRÁCA

Meranie asférických optických plôch pomocou
štandardných detektorov vlnoplochy



Vypracovala	Bc. Sandra Drusová
Obor	Optika a optoelektronika
Vedúci práce	Mgr. Bohumil Stoklasa
Dátum odovzdania	28. apríl 2014

PALACKÝ UNIVERSITY, OLMOUC
FACULTY OF SCIENCE
DEPARTMENT OF OPTICS

MASTER THESIS

Aspherics optical shop testing with standard wavefront
sensors



Written by	Bc. Sandra Drusová
Study program	Optics and Optoelectronics
Supervisor	Mgr. Bohumil Stoklasa
Date	April 28, 2014

The Declaration

I declare I have written this thesis myself under the guidance of my supervisor Mgr. Bohumil Stoklasa. Further I declare that I have used the literature I have cited.

Olomouc, April 28, 2014

.....
Bc. Sandra Drusová

Aknowledgements

I would like to thank my supervisor, Mgr. Bohumil Stoklasa, for his patient guidance and feedback to my work. This thesis would not have been possible without colleagues from Measurement methods development department in MEOPTA who helped me in my supervisor's absence. I must express my gratitude to Daniel Vacula, Milan Matela and Josef Hnilo working in Optical engineering department in MEOPTA, who gave me lectures about optical design. Special thanks goes to Peter Klein and Marta Straková for their help when my computer broke down few days before finishing my work.

Abstrakt

Cieľom práce je zhodnotiť možnosti testovania asférických šošoviek v spoločnosti MEOPTA - optika, s.r.o. Budú použité dve dostupné zariadenia, Shack-Hartmannov senzor a Fizeau interferometer. V práci je navrhnutá metóda testovania rotačne symetrických asfér bez dodatočnej nulovacej optiky. Účinnosť a obmedzenia navrhutej metódy sú experimentálne overené meraním na Fizeau interferometri. Pre budúce aplikácie boli taktiež navrhnuté jednoduché nulovacie kompenzátory.

Abstract

This thesis describes the possibilities for aspherical lens testing in company Meopta - optika, s.r.o. The suitability of two available devices Shack-Hartmann sensor and Fizeau interferometer is compared by simulating and testing of real aspheres. Method for testing of rotationally symmetric aspheres without a null optic is proposed. In order to extract the information about the surface deformations, shape of detected wavefront is predicted by theoretical calculations. Efficiency and limitations of the method are experimentally checked on Fizeau interferometer. Simple refractive null compensators were designed for the future measurements.

Contents

1	Introduction	2
2	Testing of Aspherical Wavefronts and Surfaces	4
2.1	Mathematical Representation of Aspherical Surfaces	5
2.1.1	Wavefront Description with Zernike Polynomials	6
2.2	Methods for Aspherical testing	7
2.2.1	Optical Profilometers	7
2.2.2	Adapted Wavefront Testing	8
2.2.3	Multiple Wavelength Interferometry	10
2.2.4	Subaperture Stitching Interferometry	11
2.2.5	Non-adapted Wavefront Testing	12
2.3	Measuring Instruments	13
2.3.1	Newton Interferometer	13
2.3.2	Twyman-Green Interferometer	13
2.3.3	Fizeau Interferometer	14
2.3.4	Shack-Hartmann Sensor	16
2.4	Phase Shifting Interferometry	18
2.4.1	Phase Unwrapping	20
3	Shack-Hartmann Sensor vs. Phase Shifting Interferometry	23
3.1	Comparison	23
3.2	Simulation	25
3.3	Discussion	28
4	Non-null Testing	29
4.1	Measurement Procedure	30
4.2	Computer Program for Theoretical Simulations	33
4.3	Theoretical Limits of Intellium Interferometer	36
4.4	Comparison of Unwrapping Algorithms	38
4.5	Experimental Verification of Nyquist Condition	41
4.6	Non-null Testing Results	42
4.7	Discussion	49

5 Retrace Error 50
5.1 Experimental Approach 51
5.2 Theoretical Approach 53
5.3 Discussion 57

6 Null Testing 59
6.1 Optical Design and Tolerancing 59
6.2 Null Compensators for Aspheres 61
6.3 Optimization Results 62
6.3.1 Reflectivity of Aspherical Surface 66
6.3.2 Tolerance Analysis 66
6.3.3 Mechanics for Null Component 70

7 Conclusion 72

A List of Aspheres Used in MEOPTA 74

B Zernike Frindge Coefficients 76

C LENS 7: Measurement Protocol from Asphericon 77

D LENS 6: Mechanics for Null Compensator 78

Chapter 1

Introduction

This master thesis will focus on describing the possibilities of testing surface quality of aspherical lenses using technologies available in MEOPTA-optika, s.r.o. Aspherical lenses will be tested using HASO Shack-Hartmann sensor and ESDI Intellium interferometer. The goal is to identify the limitations of both devices, experimentally and theoretically. Theoretical simulations will be performed on a sample of eleven aspheres used in MEOPTA products. The efficiency of suggested methods for aspherical testing will be discussed based on results.

MEOPTA uses aspheres in wide range of products, but still cannot manufacture its own aspherical lenses in Přerov. The aspherical lenses have to be ordered from other manufacturers, therefore it is important to have a method how to test the surface quality. Aspherical lenses are tested together with other optical elements of the system. If the system performance does not meet the expectations, usually the problem is caused by an aspherical lens. The unsatisfactory lens is sent back to the manufacturer for additional testing. Having an accurate, economical and reliable measurement method will certainly become a powerful tool in MEOPTA's hands. Measuring the aspherical surfaces is more complicated compared to the spherical surfaces and requires expensive beam shaping optics or special techniques. Such kind of solution is not always necessary, so in this master thesis, we are trying to determine if available aspheres can be measured using conventional methods.

Chapter 2 gives an overview of current aspherical testing methods, instruments and phase shifting interferometry as an important interferogram analysis method.

Chapter 3 includes a theoretical comparison between Shack-Hartmann sensor and interferometric phase shifting algorithm for reconstruction of an aspherical wavefront. In the simulation, wavefront is directly imaged on high resolution CCD chip and sampled by microlenses at the same time. The limitations of both wavefront detection techniques are found.

In the next chapter, Non-null Testing, a procedure for aspherical testing using Intellium interferometer is described in detail. The limits of algorithms reconstructing the wavefront from interferograms are checked, performance of all available algorithms is compared. Section 4.2 includes the description of program performing the theoretical simulations.

The error introduced by interferometer optics is further discussed in Chapter 5. Experiments with defocused spheres and theoretical simulations on Twyman-Green interferometer are performed to determine its influence on the measurement.

In Chapter 6, a simple compensator that adapts the wavefront to the shape of the surface under test was designed for three aspheres. The compensator for the asphere with the highest coefficient of asphericity was chosen to be manufactured. Since the degree of compensation critically depends on the distance between the compensator and the asphere, mechanical device which secures the position of both elements was designed as well.

Chapter 2

Testing of Aspherical Wavefronts and Surfaces

Aspherical surfaces have become the solution of choice in modern high-end optics. Spherical lenses are still widely used in optical systems because of existence of simple methods how to manufacture and measure them. The advantage of aspherical elements, compared to classical spherical or planar optics, is the highly increased degree of freedom for the optics design. Using aspherical elements brings more benefits, for instance, it allows the straight-forward aberration correction. Aspheres are powerful in correcting not only the spherical aberration, but also field-dependent off-axis aberrations. Besides that, they can considerably reduce the number of optical elements and therefore, size and weight of an optical system. a single asphere offers the same amount of correction that two or more spherical lenses can accomplish. This leads to more compact and lightweight systems with higher optical performance. Mentioned benefits caused the aspheres are widely used in the state of art optical systems, including lithography, space applications, fluorescence microscopy, atmospheric optics or common imaging systems for cameras in mobile phones, CD players, and even more.

If the rotational symmetry of the aspherical surface is broken, more degrees of freedom are available for the optics design. Those so called free-form surfaces are perfect for the systems where the elements are no longer arranged along a straight line, but where the optical axis is folded [1]. One of the advantages of off-axis systems with free-form surfaces is the absence of reflexes that often occur at the center of the lens in the on-axis systems. This problem usually appears when working with coherent light sources. Choosing the free-form surfaces allows the construction of more compact systems which are less vulnerable to mechanical stress or vibrations.

In general, aspheres can be manufactured with higher numerical aperture (NA) than traditional lenses. This fact was proved to be extremely beneficial in focusing and collimating the light. Using the asphere instead of sphere in a lens design can bring the spot size closer to diffraction limit. Due to the high NA (low F#) capabilities aspherical lenses provide much higher throughput through an optical system. One of the applications is the fluorescence microscopy, where the amount of collected light is often minimal. Aspherical lenses with high numerical aperture are also a perfect

solution for coupling light into fibers. Spherical lens with the same numerical aperture suffers from the high spherical aberration.

Aspheres can be manufactured out of different materials, ranging from glasses, plastics to crystalline materials and metals. The selection of material depends on the method with which it will be made. The conventional methods for manufacturing spherical optics can no longer be applied, that is why the cost of aspheres is much higher. Small glass or plastic aspherical lenses can be made by molding, which allows economical high volume production[2]. Larger aspheres are made by grinding and polishing. The approaches to aspherical polishing are based on the principle of trying to imitate spherical polishing. First, the right form is roughly shaped in the material, then polishing gives it the final shape. The surface is polished with a lap flexible enough to polish the changing curvature of the asphere. Figure errors need to be checked multiple times during the process. For a small amount of high precision aspherical lenses, diamond turning is the most common method [3]. In a single-point diamond turning, computer-controlled lathe with a diamond tip cuts the desired profile and achieves sub-micrometer accuracy. Diamond turning is limited by the strength of the used material. This method is commonly used for producing infrared optics, but due to magnetorheological finishing (MRF) [4] the visible optics can be produced as well. Other finishing methods that remove the material to reach the desired accuracy include ion-beam finishing and abrasive water jets[5].

All the processes have to be properly controlled by other measurements, so a surface can only be manufactured as precise as it can be measured. Finding the reliable and universal measuring method is a challenge for optical engineers and designers.

2.1 Mathematical Representation of Aspherical Surfaces

The most common shape of optical surface is spherical, described by sag equation

$$z_s = R - \sqrt{R^2 - r^2}, \quad (2.1)$$

having the radius of curvature R and radial coordinate $r = \sqrt{x^2 + y^2}$ ranging from $-d/2$ to $d/2$, where d is the surface diameter. Because this representation fails for flat surfaces, a better and more general form of the previous equation is

$$z_s = \frac{c \cdot r^2}{1 + \sqrt{1 - c^2 \cdot r^2}}, \quad (2.2)$$

where $c = 1/r_s$ is the curvature. This equation is still missing the parameters describing conic surfaces. Conic constant as eccentricity squared $K = e^2$ is inserted into the equation as follows:

$$z_s = \frac{c \cdot r^2}{1 + \sqrt{1 - (K + 1)c^2 \cdot r^2}}. \quad (2.3)$$

K defines the type of the conic surface, see Table 2.1.

Type of conic surface	Conic constant value
Hyperboloid	$K < -1$
Paraboloid	$K = -1$
Ellipse rotated about its major axis (prolate spheroid or ellipsoid)	$-1 < K < 0$
Sphere	$K = 0$
Ellipse rotated about its minor axis (oblate spheroid)	$K > 0$

Table 2.1: List of conic surfaces [6]

An asphere is an optical surface differing from a sphere. In this thesis, we will work only with the rotationally symmetric elements. Compared to a sphere, general equation describing an asphere contains some additional terms, usually not more than three. Asphere can also be derived from a surface with a non-zero conic constant. Its equation is then

$$z_a = \frac{\frac{1}{r_a} \cdot r^2}{1 + \sqrt{1 - (K + 1) \left(\frac{1}{r_a}\right)^2 \cdot r^2}} + \sum_{i=1}^n A_i r^{2i}, \quad (2.4)$$

where r_a is vertex radius of curvature and A_i are the aspherical deformation coefficients.

2.1.1 Wavefront Description with Zernike Polynomials

In optical systems with rotational symmetry, wavefront can be expanded in terms of a complete set of Zernike polynomials which are orthogonal over unit circle. Each polynomial represents the aberration of the system with circular or annular pupil.

Arbitrary shape is constructed of linear combination of basic shapes

$$W(r, t) = \sum_{n=0}^{\infty} \sum_{m=0}^n c_{nm} Z_n^m(r, t), \quad (2.5)$$

where c_{nm} are the expansion coefficients, n and m are positive integers including 0 ($n - m \geq 0$ and even),

$$Z_n^m(r, t) = \sqrt{2(n+1)/(1+\delta_{m0})} R_n^m(r) \cos(mt) \quad (2.6)$$

are Zernike polynomials with radial part defined as

$$R_n^m(r) = \sum_{s=0}^{(n-m)/2} \frac{(-1)^s (n-s)!}{s! \left(\frac{n+m}{2} - s\right)! \left(\frac{n-m}{2} - s\right)!} r^{n-2s}. \quad (2.7)$$

When the wavefront is known only at the discrete set of points (due to pixelated structure of CCD chip), Zernike polynomials are not orthogonal over the obtained data. Values of coefficients are not independent of each other and the result depends on number of polynomials used for wavefront decomposition. The accuracy is connected to the number of data points.

Mathematically, with surface data set of M points and N Zernike polynomials, polynomial expansion is solving an overdetermined system of equations:

$$W = Z \cdot c. \quad (2.8)$$

The columns of Z are formed by individual Zernike polynomials evaluated at each grid point. An optimal solution in the least squares sense is the one minimizing a vector of residuals

$$\begin{pmatrix} e_1 \\ \vdots \\ e_N \end{pmatrix} = \begin{pmatrix} Z_{11} & Z_{12} & \dots & Z_{1N} \\ \vdots & \vdots & \ddots & \vdots \\ Z_{M1} & Z_{M2} & \dots & Z_{MN} \end{pmatrix} \cdot \begin{pmatrix} c_1 \\ \vdots \\ c_N \end{pmatrix} - \begin{pmatrix} W_1 \\ \vdots \\ W_M \end{pmatrix}. \quad (2.9)$$

Unknown Zernike coefficients are Moore-Penrose pseudo-inverse least-squares solution to (2.8) [7]:

$$\begin{pmatrix} c_1 \\ \vdots \\ c_N \end{pmatrix} = (Z^T \cdot Z)^{-1} \cdot Z^T \cdot \begin{pmatrix} W_1 \\ \vdots \\ W_M \end{pmatrix}. \quad (2.10)$$

2.2 Methods for Aspherical testing

Aspherical surface, like any other optical surface, might be damaged by contact measurement, so it is mostly measured optically. If there is a high quality reference surface available, it is possible to do a null test. The necessary precondition for any null test is the existence of system configuration, in which the difference between reference and test wavefront approaches zero. In order to achieve that, additional components may need to be placed in the optical system to modify the wavefront. There are two types of null components: refractive, such as single lens, multiple lenses, or diffractive, i.e. computer generated hologram. Non-null methods, where the null condition is violated, are often cheaper, more universal, although their accuracy is subject for discussion. For weak aspheres with low deviation from sphericity, common interferometers like Twyman-Green and Fizeau together with phase shifting wavefront reconstruction technique can be used. In order to overcome a problem with large deviation from sphericity, an aperture is divided into smaller sub-apertures measured separately. The separate measurements all sub-apertures are stitched together, thus the technology is known as aspherical stitching interferometry. Insufficient detector sampling for interferometric measurements will not cause aliasing of interferograms if a longer test wavelength is used.

2.2.1 Optical Profilometers

Profilometry is a technique used to extract information about surface topology. In optical profilometry, light is used instead of physical probe for non-destructive measurement. a surface can be divided into discrete set of points, a grid, and slowly mapped point by point. One of the point scanning techniques is called confocal profilometry. The light from the source is projected through

the aperture and focused on the sample. The system scans in the vertical direction to get the bright spot from light reflected from the surface. The signal on the camera is the most powerful when the aperture lens is properly focused on the sample. The height of the surface is calculated in this point, then the probe scans the sample laterally to get 3D data. One of the devices using this principle is confocal microscope.

2.2.2 Adapted Wavefront Testing

A null test is usually defined as a procedure of producing a fringe-free field during interferometric testing. The wavefront in the system is adapted to the shape of tested element. Due to the imperfections of optics involved in the test, interference fringes will appear. If the null optic is perfect, any tilt or tested surface deformation can be recognized from the density and the shape of the fringes.

Null testing of spheres is quite straightforward: a precise transmission sphere is used to create spherical wavefront, which is compared to the surface. Putting the center of curvature of the surface coincident with the focus position of the transmission sphere, the light is retroreflected.

The transmission asphere is not always necessary for null measurements of aspheres. Conic surfaces always have a pair of conjugate foci that image the point source without spherical aberration. Purely conic aspheres, defined only by conic constant, are called stigmatic surfaces. If they are illuminated by convergent/divergent spherical wave having the centre of curvature identical to one of the foci, the reflected wave is spherical and thus easier to test. In other words, they form a perfect image of the point source in certain configuration. In case one of the foci is inaccessible, auxiliary optical elements are required. For conic surfaces such as paraboloids, hyperboloids and ellipsoids, more tests are available. a convex hyperboloidal surface can be tested with the method proposed by Hindle. The similar setup can be used for testing of concave ellipsoidal surfaces. Silvertooth found an useful way how to test small concave hyperboloids. If a large reference flat surface is available, two mirror Cassegrain telescope can be tested in Ritchey's configuration (see Figure 2.1).

Even though all the mentioned tests are very important in astronomy, they are not an universal method for aspherical testing. Unfortunately, the majority of conic aspherical surfaces also has non-zero values of aspherical coefficients, so the tests would fail.

More general solution for aspherical testing is to introduce a correction optics which modifies the incoming wavefront in such way that it resembles the tested surface. An additional inserted element is called **null corrector** or **null compensator**. The null compensator reshapes the beam, so it hits the test sample nearly perpendicularly. Null optical components are also aberrated and have to be calibrated. It is necessary to manufacture the null corrector with higher level of accuracy than it is desirable for tested surface. This demand is sometimes too high to satisfy in case the compensator contains an aspherical surface, so this is why the components of null compensator are mostly spherical or flat. Furthermore, different types of aspheres require own custom-made null components, which is the reason why aspherical testing is so expensive and time-consuming.

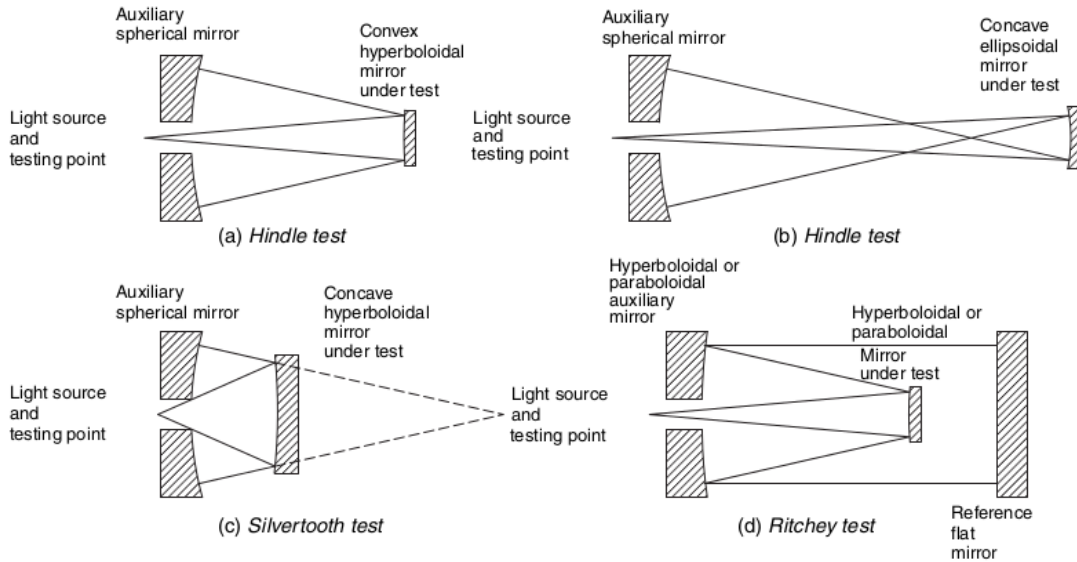


Figure 2.1: Several null tests of conic surfaces, picture from [8]

Null compensators may be implemented with refractive, reflective (e.g. auxiliary mirrors in Hindle test in Figure 2.1) or diffractive optics. Due to rotational symmetry of aspherics, the spherical aberration is often dominant in a system. Reducing the spherical aberration makes the testing much easier and more methods can be applied. Refractive compensators (lenses) compensate the spherical aberration with different degree of precision. Several different configurations were proposed by Dall [9], Shafer [10] or Offner [11]. All can be used in single or double pass. The amount of aberration correction strongly depends on the position of compensating element; it must be set very accurately. The general smoothness of the surface can be easily determined only with a compensator.

A diffractive null component is called **computer generated hologram (CGH)** [12, 13]. Unlike in conventional holography, the object does not have to physically exist. Hologram is nothing else than interferogram with large tilt between the reference and object wavefront. Holograms are recorded onto photographic plates, thermoplastic materials or in photorefractive crystals. After the hologram is developed, it is put in the exact same position as before and illuminated by the reference wave. It is basically a grating diffracting the incoming light into several diffraction orders, but we are interested only in +1 and -1, which is the reconstructed object wave and its complex conjugate. The spatial filter is needed to select only one diffraction order.

Using the computer program, the hologram structure can be precisely calculated if the system properties are known (including all aberrations). a CGH is a binary representation of the real hologram. CGH should be made in a plane conjugate to the exit pupil of the system under test. For testing, the CGH is put in the same position as the real hologram. Illuminated correctly by the plane wave, it provides the perfectly shaped reference wavefront emerging on the surface under

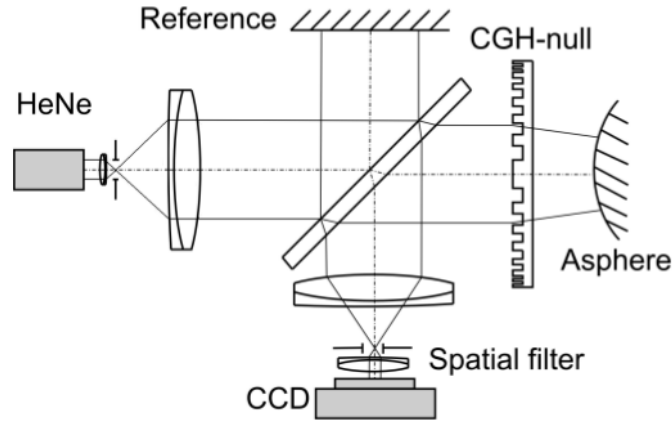


Figure 2.2: Twyman-Green interferometer setup for testing of asphere with CGH [14]

test. Any differences between reference and test object will appear on the screen if the effects of the interferometer and the CGH are known. One setup for holographic testing of aspherical mirror is shown in Figure 2.2. The holograms can be used in both in-line and off-axis configurations, see for example [15]. CGH have many advantages over refractive compensators: lower cost, short delivery time, almost arbitrary wavefront generation. Together with refractive/reflective null optics, more complicated aspheres can be measured, as well as freeform surfaces [16].

The calibration of CGH is not trivial; manufacturing tolerances introduce phase errors. To identify parameters with a significant influence on the generated phase, rigorous sensitivity analysis has to be done for typical gratings [17]. The optimal design of CGH blazed microstructures is suggested by Peterhänsel et al. [14], Zhou and Burge [18].

2.2.3 Multiple Wavelength Interferometry

A single wavelength interferometry, as a technique to describe the surface of optical elements, is limited by detector sampling size or sensitivity. If a resulting interferogram contains too many fringes to analyze by phase-shifting technique described in section 2.4, one solution to this problem would be the change of working wavelength. The longer the wavelength, the wider are the fringes; the dynamic range of the device can be increased. However, there might not be a detector available working on this wavelength, so the fringes cannot be displayed directly. Two or multiple-wavelength holography is a way how to get an interferogram with longer effective wavelength using visible light sources.

The longer wavelength can be synthesized by simultaneously using both wavelengths in the interferometer. The second option would be first recording the fringes obtained by visible light with λ_1 on photographic film. The photographic recording (hologram) is then developed and placed in the same position as it was during the exposure. After that, it is illuminated by different wavelength λ_2 . The resulting interferogram represents the interference between the test wavefront stored in hologram and the test wavefront currently measured with λ_2 . Phase difference for superposition of the two wavelengths is

$$\Phi_2 - \Phi_1 = 2\pi \left(\frac{1}{\lambda_2} - \frac{1}{\lambda_1} \right) OPD = \frac{2\pi}{\lambda_e} OPD. \quad (2.11)$$

The envelope of the fringes is the interferogram that would be obtained when illuminating the tested surface with one effective wavelength

$$\lambda_e = \frac{\lambda_1 \lambda_2}{|\lambda_1 - \lambda_2|}. \quad (2.12)$$

A suitable source for this method is CO₂ laser operating at number of different wavelengths.

2.2.4 Subaperture Stitching Interferometry

The need of new technology has become urgent for testing large aspherical diameters [19, 20]. Better than expensive large-aperture interferometers and transmission spheres, subaperture stitching has become more elegant solution. Nowadays, stitching is the way how to measure the aspheres with big departure from spheres, which cannot be measured using conventional interferometers because of insufficient detector sampling. The large aperture is divided into smaller overlapping subapertures and individual measurements are stitched together to give the final aspherical shape. Stitching expands the measurement capability of conventional interferometers. Each subaperture can have its own measurement conditions; by choosing the correct subaperture shape the process might be faster and easier.

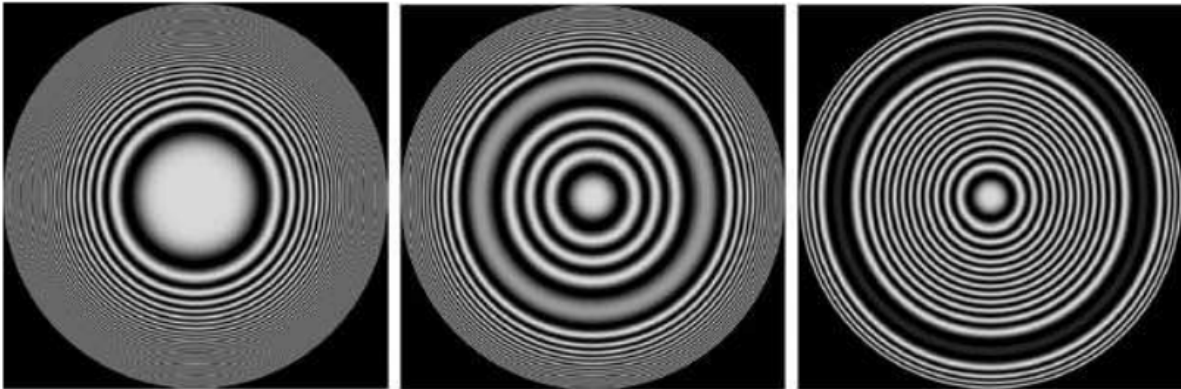


Figure 2.3: Illustration of annular subaperture testing [8]

One approach uses annular subapertures and Fizeau interferometer [21, 22, 23]. At first, the asphere is placed in the position where the reference beam curvature coincides with its vertex radius of curvature. Only the central part gives resolvable fringes, others are too dense at the edges. By varying the distance between the asphere and the focus of the transmission sphere, the slope of the reference wavefront changes and matches the slope at the outer parts (see Figure 2.3). The null zone slowly moves from the centre toward the edges. The measurements are taken in each overlapping null zone and translation errors are simultaneously eliminated by least-squares fitting.

The other technique uses circular subapertures where the tilt, defocus, local curvature and transmission sphere magnification are optimized to give the lowest fringe density. The size and number of subapertures, so called lattice, is calculated by the computer program [25]. Since the apertures are measured off-axis, the aberrations present in the interferogram will be mostly astigmatism, coma and trefoil. Therefore, a device able to variably generate those aberrations in different amounts to null the fringes as much as possible was designed. Variable optical null device [26, 27] consists of two nominally identical, rotatable optical wedges, which are easy to manufacture, calibrate and align. The disadvantage of subaperture stitching is mainly its long measurement time when the number of subapertures is quite large.

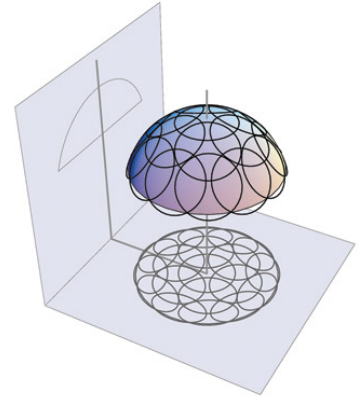


Figure 2.4: Circular subapertures for aspherical testing [24]

2.2.5 Non-adapted Wavefront Testing

If testing the aspheres with aspherical wavefront is not available, plane or spherical wavefront is used instead. Non-adapted testing is realized only in case of rotationally symmetrical aspheres, otherwise alignment problems would be significant. The method also relies on a-priori information about the smoothness of the tested surface. Taking into account the nature of grinding and polishing processes, all the deformations from ideal shape are smooth. Systematic errors appear as a consequence of inability to meet the null test condition. Basic interferometric setups are Newton, Twyman-Green and Fizeau interferometer. The interferogram data are usually analyzed by phase shifting method (section 2.4). Alternatively, wavefront can be detected by Shack-Hartmann sensor.

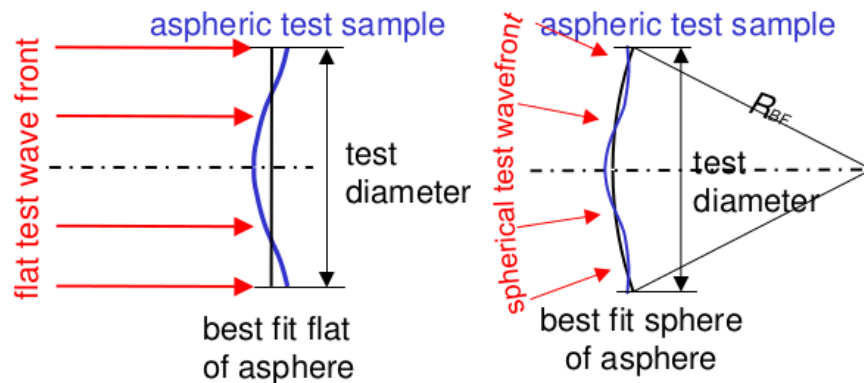


Figure 2.5: Non-adapted planar and spherical wavefront used in aspherical testing, picture from [28]

2.3 Measuring Instruments

2.3.1 Newton Interferometer

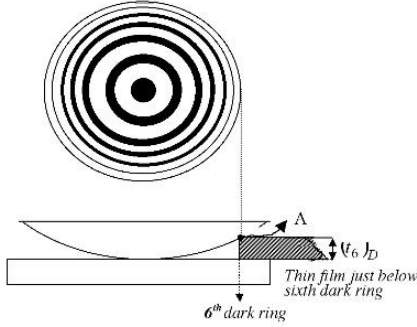


Figure 2.6: Newton rings observed for spherical surface lying on the optical flat [29]

coordinate are viewed by measuring microscope. An asphere measured this way can have a large deviation from the nearest sphere, around 20λ . Both surfaces should have their optical axes aligned in such way that they coincide.

Two optical surfaces in close contact illuminated by monochromatic light can be considered as Newton interferometer. The light incident on the first glass-lens boundary is partially transmitted and partially reflected. The light that is transmitted to the air travels a certain distance before it is reflected at the flat surface below. Both reflected rays interfere and create so-called Newton fringes.

Newton fringes method can be applied to aspherical surface measurements as well. An asphere is placed on a sphere with nearest diameter. The fringes representing the thickness of the air gap as a function of radial

2.3.2 Twyman-Green Interferometer

Twyman-Green interferometer is an example of two-way interferometers, where a final interferogram is created by superimposing reference and test wavefront. Setup is adjusted to measurement of a single surface. In the basic configuration, light from the laser is collimated by collimating lens or microscope objective. Half of the light is reflected by beam splitter and reflected back by reference mirror, the other half goes into the test arm.

In this type of interferometer, the requirements on the quality of beam splitter are very high. The material must be very homogeneous, the surfaces must be very precisely manufactured. The reflective surface must be extremely accurate. The other non-reflective surfaces are antireflection coated in order to prevent unwanted reflections. Another method how to get rid of the reflections is to tilt the beam splitter in such way that incidence angle is equal to Brewster angle and give the reflection a different polarization.

Twyman-Green interferometer can be used for testing of aspheres, usually the reference surface is a planar mirror. This type of interferometer is more flexible for measurement of coated surfaces due to possibility of contrast adaptation.

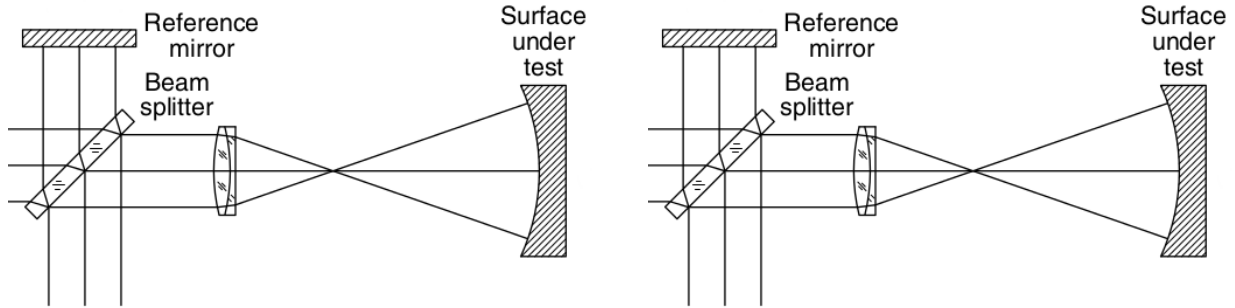


Figure 2.7: Testing convex (left) a concave (right) spherical surface with planar reference [30]

2.3.3 Fizeau Interferometer

Fizeau interferometer is a very popular instrument in the area of optical testing. Compared to Newton interferometer, the air gap between tested and reference surface in Fizeau interferometer is much larger. One advantage of this arrangement is that surfaces do not need to be cleaned as properly as in Newton interferometer. On the other hand, the large air gap imposes requirements on coherence of illuminating light source. Nowadays, coherence length of few meters can be achieved with commercially available lasers. However, large coherence length can cause an interference between the reference wavefront and an unwanted reflection from other surfaces in the system.

A key element of Fizeau interferometer is so called transmission flat or transmission sphere. Transmission sphere converts the wavefront from laser source to a perfectly spherical wavefront. The last surface of the transmission sphere is concentric to the focal point of transmission sphere and it is manufactured with the highest level of accuracy. All surfaces in the transmission sphere are antireflection coated except the last one. The reference wavefront is reflected from the last surface and interferes with the wavefront reflected from the test. The last surface is basically a beam splitter. Wavefront is imaged onto CCD detector, usually with resolution around 1000x1000 pixels.

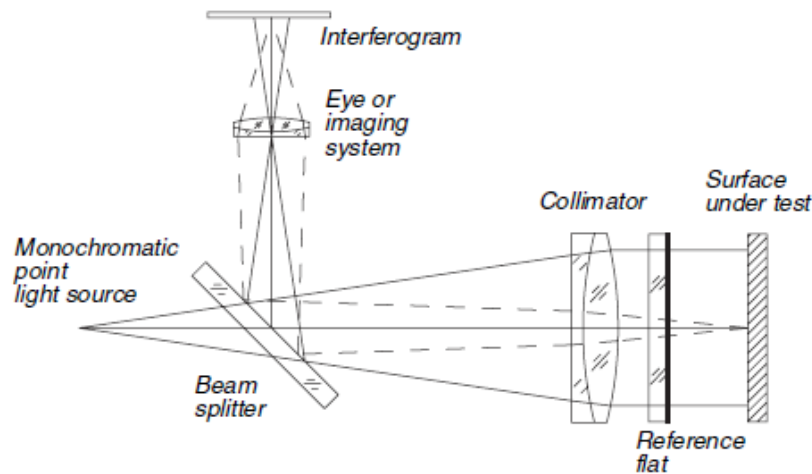


Figure 2.8: Testing flat surface on Fizeau interferometer [8]

When measuring flat surfaces, light from a point light source needs to be collimated by lens or

mirror. The reference flat must be adjusted so the image of the pinhole falls on the pinhole itself. The side of the reference flat, which is not important in the measurement, should be antireflection coated or tilted to suppress or deflect the reflected light. a beam splitter between the point light source and reference surface allows to see the fringes from the side using CCD camera. Negative lens in setup shown in Figure 2.8 projects the fringes on the screen as well. Removing it from the system facilitates primary adjustment. Pinhole image of the reference surface appears in the middle of the screen, test surface is imaged at a different position. Two surfaces are aligned parallel to each other when their pinhole images coincide.

Collimated laser beam used for testing flats on Fizeau interferometer can be easily transformed into a convergent or divergent one by transmission sphere, and therefore used for testing of curved surfaces. This method relies on the fact that any ray from the center of curvature of the sphere is reflected back following the same direction. Figure 2.9 shows an arrangement for testing spherical surfaces with concave reference sphere (the null test).

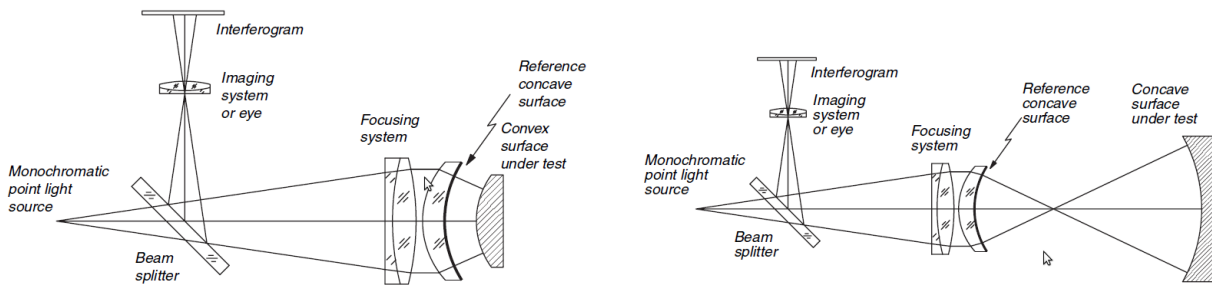


Figure 2.9: Testing convex (left) and concave (right) spherical surface with concave reference [8]

Before any measurements, it is important to choose the reference sphere with suitable numerical aperture; tested sphere should be fully illuminated. Focal length of the reference transmission sphere must be obviously larger than the radius of convex surface in the current arrangement (Figure 2.9). The next step would be to localize the focal point of the reference lens and place the tested surface in this position. Additional tilt adjustments should be leading to an interferogram known as the cat's eye (Figure 2.10).



Figure 2.10: Interferogram at the cat's eye point

Using additional measurement device it is necessary to move the sphere by an exact distance corresponding to its radius of curvature. The aim is to align two spheres in the system so their centers of curvature coincide. Then we want to achieve the uniform air gap between them. The wavefront reconstruction is usually made by phase-shifting technique. OPD directly corresponds to the manufacturing distortions of the surface.

Aspheres can be measured using Fizeau interferometer, but the possibilities are limited. After

localizing the best test position, data need to be corrected for non-null test errors. The local normal of the aspherical surface and the incidence direction of the rays include the angle α so the reflected ray deviates 2α from the original direction. The direction of reflected rays might be changed so much that it can no longer pass through the system aperture, so in the end, some zones of the test surface are not visible on the detector at all. The issue is often a high fringe density, that is why the detectors with high resolution CCD chip are used. The influence of chip resolution is described in subsection 2.4.1. Aspherical non-null testing will be further studied in chapter 4.

2.3.4 Shack-Hartmann Sensor

The predecessor to the Shack-Hartmann sensor was Hartmann's screen test, where a mask with large number of holes is placed over primary mirror of a telescope. The telescope is pointed at a star and a detector is placed in a focal plane of the mask. Several subimages are formed and their displacement over a long time is directly proportional to the gradient of wavefront change.

Since 1980s, the CCD chips are used as light detectors replacing photographic plates. In the wavefront analysis, the plate was simultaneously exposed to a perfect plane wave and aberrated wave to be measured. Plane wave formed reference spots on the plate, and the displacement of spots of test wave had to be measured manually after development. This painstaking procedure was rewarding for astronomers - aberrations of telescopes could be measured using unfiltered star light. Effects of atmospheric turbulence are averaged over a long exposure time, so they do not cause any problems in the measurements.

Mask with holes was later replaced by microlens array, usually with around 100x100 microlenses. All microlenses are identical, they have the same focal length. Each one of them focuses the corresponding part of an inspected wave on CCD chip located at the focal plane of lenslet array. The geometrical shift of the point spread function reveals the information about wave aberrations of the incident wave. Position of the focused spots depends on the average wavefront slope taken across the respective microlens aperture of the Shack-Hartmann sensor. The relationship between the slope $W'(x)$ and spot displacement Δx depends on the focal length f :

$$\Delta x = f \cdot W'(x) \tag{2.13}$$

The local slopes are patched together to reconstruct a complete wavefront over the aperture of the sensor. The diameter of the beam is usually adapted to the S-H aperture using beam expanders/reducers, reaching a fill factor around 70-90 %. In the simplest case, aperture of each microlens has a quadratic shape, so there are no dead areas on the sensor. Apertures can also be hexagonal or circular.

The sensor is described by several parameters:

- the number of microlenses (subapertures) N

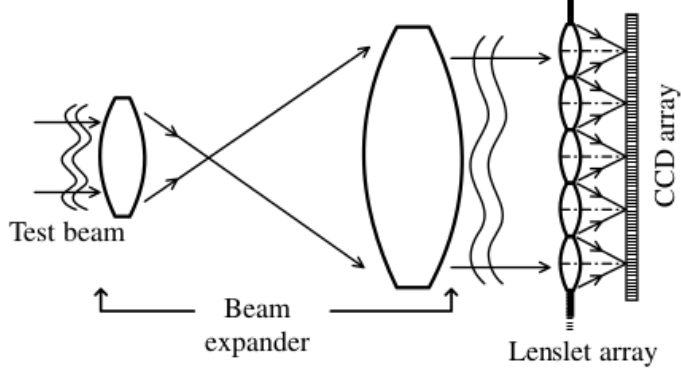


Figure 2.11: Principle of Shack-Hartmann wavefront sensor [31]

- Size of each subaperture d_A
- Focal length of an array f
- Beam aperture relative to array aperture = fill factor F
- CCD pixel size p

Wavefront reconstruction can be described in two steps. At first, the position of the shifted spot is determined by centroiding algorithms, then the total wavefront is reconstructed from local slopes. Most of the wavefront reconstruction error arise from inaccurate centroiding, therefore it is very important to precisely locate the center of the spot.

Multiple centroiding algorithms are available. If the beam intensity is high, the most basic approach is to calculate the centre of gravity. Position of the centroid is a weighted mean of spot coordinates, where the weights are the spot intensities corresponding to the coordinates. Centroid position is found by averaging in the area as large as the subaperture of one microlens.

$$(x_c, y_c) = \left(\frac{\sum_{i,j=1}^N I_{i,j} x_{i,j}}{\sum_{i,j} I_{i,j}}, \frac{\sum_{i,j=1}^N I_{i,j} y_{i,j}}{\sum_{i,j} I_{i,j}} \right), \quad (2.14)$$

where N is the number of pixels.

In some cases, with the shape of spot being known, this a priori information can be implemented into centroiding algorithm as a weighting function w

$$(x_c, y_c) = \left(\frac{\sum_{i,j=1}^N w_{i,j} I_{i,j} x_{i,j}}{\sum_{i,j} w_{i,j} I_{i,j}}, \frac{\sum_{i,j=1}^N w_{i,j} I_{i,j} y_{i,j}}{\sum_{i,j} w_{i,j} I_{i,j}} \right). \quad (2.15)$$

Weighting function can have a gaussian shape or it can be a square of an spot intensity distribution. Very precise centroiding position is found iteratively; the weighting function changes every iteration. It is modified in such way that it becomes centered around the new centroid location. The initial iteration uses gaussian function.

The Matched Filter Centroiding algorithm measures the centroid location by maximizing the cross

correlation of the spot with its predicted position.

The next step after finding the centroid position is found is the numerical wavefront reconstruction. The gradient of an unknown wavefront defined at grid of points is numerically integrated, using for example trapezoidal rule.

$$W = W_x + W_y, \quad W_x = \frac{1}{f} \int_0^x \Delta x \, dx, \quad W_y = \frac{1}{f} \int_0^y \Delta y \, dy \quad (2.16)$$

In different method wavefront is computed by least-squares fitting with derivatives of Zernike polynomials.

2.4 Phase Shifting Interferometry

With the beginning of computer era, the problems of getting an interferogram into the digitized form and analyzing it properly naturally appeared. One of the most commonly used techniques nowadays is the Phase shifting interferometry (PSI). PSI can be considered as a data analysis method useful in a great variety of situations. The applications include optical testing, real-time wavefront sensing for active optics, and microscopy.

PSI has some significant advantages over static interferogram analysis. For static interferogram evaluation, it is essential to find the fringe centers. Most of the analyzing programs require the data spatially distributed on a regular grid, so the precision of result is decreased by necessary data interpolation. With PSI it is possible to get good results even with low contrast fringes, independent of intensity variations across the pupil. From the beginning, the data are collected along the regular grid and the measurement is fast and precise.

The fundamental concept of PSI is quite simple. Few interferograms are recorded after introducing a time-varying phase shift between the interfering beams and the unknown wavefront phase is encoded in the time changes of intensity. Reference and tested wavefront can be expressed as

$$w_r(x, y, t) = a_r(x, y)e^{i[\phi_r(x, y) - \delta(t)]} \quad (2.17)$$

$$w_t(x, y) = a_t(x, y)e^{i[\phi_t(x, y)]}, \quad (2.18)$$

where a_r and a_t are the wavefront amplitudes, ϕ_t and ϕ_r are the wavefront phases, $\delta(t)$ is the time varying relative phase shift between the beams.

The total intensity is then

$$I(x, y, t) = |w_r(x, y, t) + w_t(x, y)|^2 = a_r(x, y)^2 + a_t(x, y)^2 + 2a_r(x, y)a_t(x, y)\cos[\phi_t(x, y) - \phi_r(x, y) + \delta(t)]. \quad (2.19)$$

Defining $\phi(x, y) = \phi_t(x, y) - \phi_r(x, y)$ as wavefront phase difference, a fundamental equation describing the PSI technique can be written as

$$I(x, y, t) = I'(x, y) + I''(x, y)\cos[\phi(x, y) + \delta(t)]. \quad (2.20)$$

Resulting intensity is a time varying function of the phase shift, I' is the constant bias term, I'' is half the peak-to-value modulation. During the phase shifting process, the fringes seem to move across the field.

The most common method of introducing the phase shift is moving the internal interferometer mirror with electromagnetic or piezoelectric transducer. a plane-parallel glass or plate inserted in the light beam introduces the phase shift if it is tilted with respect to the optical axis, the diffraction grating needs to be translated perpendicularly.

The reference phase in (2.18) can be changed either continuously or in discrete steps. Continuous phase change is required when the mirror tends to oscillate after each phase step (situation when the reference surface has a large mass or the control electronics are not well damped).

Many interferogram data evaluation strategies were proposed. The series of data is acquired with discrete changes in reference wavefront phase and then, the unknown wavefront is mathematically reconstructed. One example is **four step algorithm**, where $\pi/2$ phase shift is introduced between recorded interferograms. $\delta(t)$ thus has the values $0, \pi/2, \pi, 3/2 \cdot \pi$. Substituting them into (2.20) yields four equations

$$I_1(x, y) = I'(x, y) + I''(x, y)\cos[\phi(x, y)] \quad (2.21)$$

$$I_2(x, y) = I'(x, y) + I''(x, y)\cos[\phi(x, y) + \pi/2] = I'(x, y) - I''(x, y)\sin[\phi(x, y)] \quad (2.22)$$

$$I_3(x, y) = I'(x, y) + I''(x, y)\cos[\phi(x, y) + \pi] = I'(x, y) - I''(x, y)\cos[\phi(x, y)] \quad (2.23)$$

$$I_4(x, y) = I'(x, y) + I''(x, y)\cos[\phi(x, y) + 3\pi/2] = I'(x, y) + I''(x, y)\sin[\phi(x, y)] \quad (2.24)$$

for 3 unknowns I', I'', ϕ . Fourth equation is not necessary, but it is helpful in the wavefront phase calculation. Subtracting

$$I_4 - I_2 = 2I''\sin[\phi] \quad (2.25)$$

$$I_3 - I_1 = 2I''\cos[\phi] \quad (2.26)$$

and taking the ratio of these equations the unknown phase map $\phi(x, y)$ can be computed as

$$\frac{I_4 - I_2}{I_3 - I_1} = \frac{\sin[\phi]}{\cos[\phi]} = \tan[\phi] \implies \phi = \tan^{-1} \left[\frac{I_4 - I_2}{I_3 - I_1} \right]. \quad (2.27)$$

It is straightforward to relate the phase in each grid point to optical path distance (OPD)

$$OPD(x, y) = \lambda\phi(x, y)/2\pi. \quad (2.28)$$

2.4.1 Phase Unwrapping

Now the continuous phase is sampled in discrete number of points - the arctangent function wraps the phase modulo 2π . To obtain the real phase map, the correct multiple of 2π must be added to each phase value.

$$\phi_{\text{unwrapped}}(i) = \phi_{\text{wrapped}}(i) + p(i) \cdot 2\pi \quad (2.29)$$

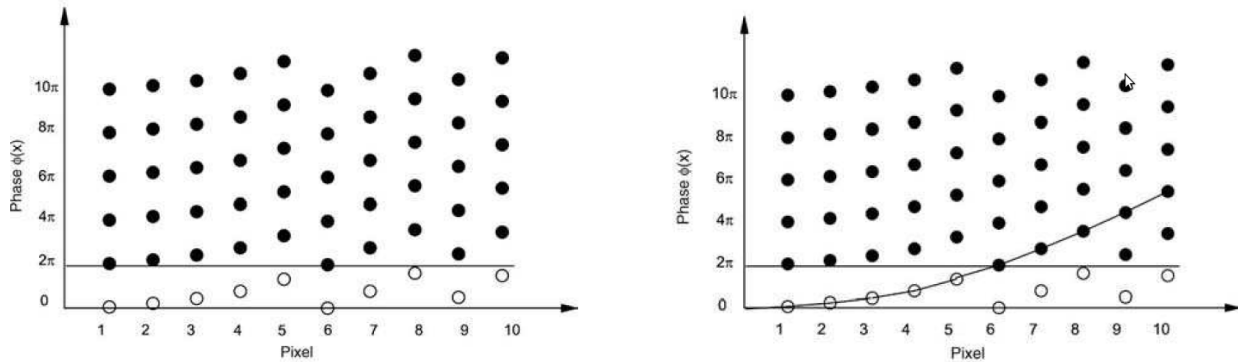


Figure 2.12: 1D unwrapping. White points are the unwrapped phase data, the black ones are few possible solutions for the unwrapped phase, curve on the right is the reconstructed phase

There are several methods how to obtain the unknown piston function $p(i)$. No standard procedure has been developed, the algorithms are the trade-off between computational time and accuracy.

The reconstruction with conventional algorithms uses a priori information about the wavefront phase change. The limit for the phase change per one pixel of CCD detector is π . Unwrapping in 2 dimensions is more complicated and the results may depend on path taken as well as the starting point for unwrapping. Thus in general, the families of conventional algorithms for unwrapping can be divided into path following algorithms and path independent algorithms.

Path following algorithms

The most simple algorithm starts from the central part and unwraps lines towards the edge. More robust algorithms choose the unwrapping path following the phase gradient or start in the region of the highest contrast first. Still they are generally vulnerable to noise propagation.

Path independent algorithms

Wrapped phase map is first clustered into regions separated by phase jumps. Path independent algorithm tries to find the best multiple of 2π to eliminate the phase jumps between all data areas. For example, Precoditioned conjugate gradient algorithm uses fast Fourier transform to iteratively solve a minimized weighted least-squares equation.

Sub-Nyquist algorithms

If the Nyquist condition is valid, and the density of fringes does not cause problems with correct phase reconstruction by conventional algorithms. With additional information about the surface, even aliased and clearly undersampled interferograms can be processed. Sub-Nyquist algorithm significantly extends the dynamic range of PSI. Sub-Nyquist algorithm assumes that the test surface is smooth, which means it has smooth derivatives.

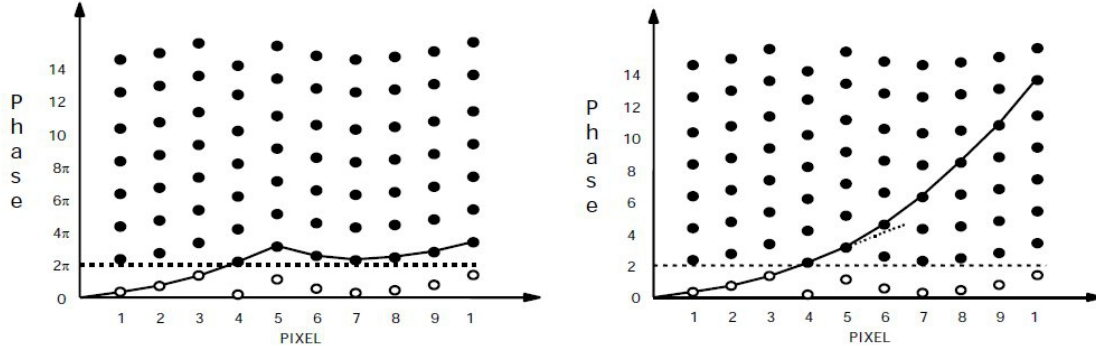


Figure 2.13: Reconstruction of the phase map violating the Nyquist condition [32]

The principle is illustrated in Figure 2.13. Conventional algorithms fail at pixel number 5, where the line slope exceeds π per pixel. Sub-Nyquist algorithm applies slope continuity constraint during the reconstruction. The correct multiple of 2π is found by extrapolating the line from previous two points, the next dot is the one closest to the extrapolated line. In case this condition is still not sufficient for smooth phase reconstruction, second order polynomial can be fitted to last three dots. In most of the cases, higher orders are not necessary. This procedure can be continued until a more fundamental limit is reached.

Sub-Nyquist algorithm is limited by pixel modulation transfer function (MTF). The detector must have a non-zero response to frequencies higher than basic Nyquist frequency. The Nyquist frequency is defined as half of the sampling frequency

$$f_N = \frac{1}{2x_s} \quad (2.30)$$

where x_s denotes pixels spacing.

Interferogram is imaged on CCD sensor, which always has an active pixel area and additional spacing for electronics. The intensity at each pixel is spatially averaged over the pixel area, resulting in the partial loss of information about the intensity modulation. The amount of lost modulation is the function of spatial frequency being recorded - the higher the frequencies, the greater the variation of intensity within the area of one pixel. First zero of MTF function is reached for the transfer of frequency $1/a$, where a is the pixel size. Therefore, in order to keep the nonzero response for wider interval of frequencies, the active area of pixels has to be reduced. One way of doing this is to use the pinhole mask for each pixel to avoid large averaging. Another possibility is choosing CCD

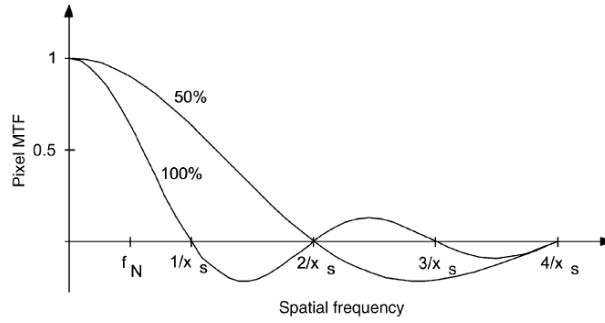


Figure 2.14: MTF for CCD chips with different width-to-pitch ratio [8]

chip with small width-to-pitch ratio which resembles the point detector. For sensors with around 10 % width-to-pitch ratio the first zero of the pixel MTF is at frequency 20 times the Nyquist frequency.

Chapter 3

Shack-Hartmann Sensor vs. Phase Shifting Interferometry

The interferometric measurement of wavefront is the most common method for testing the deformations of optical surfaces, because it provides exceptional lateral resolution. In interferometry, test and reference beam are brought together on observation plane to form the fringes. Sometimes the reference beam with the desired shape is not available, especially for testing the aspheres. In this case, using a spherical reference beam might cause problems with data analysis.

An alternative to interferometry can be a Shack-Hartmann wavefront sensor. The Shack-Hartmann sensor eliminates the need for the reference beam altogether. It has considerably lower resolution, but its insensitivity to vibration, flexibility, and the ability to measure local wavefronts over a large dynamic range are important advantages over interferometry.

This chapter will theoretically compare the limits of phase shifting interferometry and Shack-Hartmann sensor for aspherical wavefront reconstruction. Real aspheres available in MEOPTA (Appendix A) are used as test subjects.

3.1 Comparison

Shack-Hartmann (S-H) sensor has some advantages in comparison with interferometry. Interferometric measurements require a coherent light source with coherence length exceeding all distances in the system, thus the lasers are used. Measurement on S-H sensor is independent of degree of temporal coherence of the light and requires only spatial coherence. Spatial coherence will cause broadening of spots and decrease the dynamic range.

The spectral sensitivity of S-H sensor depends on the properties of CCD sensor, so in principle, all detectable wavelengths can be used if they fit into transmission interval of microlenses. Advantage for measurement of aspheres can be the possibility of using longer wavelength, which improves the dynamic range. In interferometry, usually only He-Ne laser is used.

The reason why S-H sensors are being implemented in current testing setups is reduced cost and

complexity of the setup. The requirements for perfect alignment of an interferometric setup are much higher than for Shack-Hartmann sensor. The cost of just one piece of precisely manufactured reference optics can exceed the cost of S-H sensor. S-H sensor gives the user more control over the system used for measurement in comparison with interferometry, where the parameters of commercial optics are usually not known.

In interferometry, the spatial resolution is determined by the number of pixels of CCD chip which sample the detected wavefront. S-H sensor has considerably lower resolution. The incoming wavefront is discretized by number of subapertures and changes inside one subaperture are averaged. Current CCD chip resolutions for interferometry are around 1000x1000 pixels, the number of subapertures in S-H sensors ranges from 32 to 100 microlenses in one direction. S-H sensor cannot detect wavefront errors with high frequency, it is a low pass filter smoothing the irregularities of the wavefront.

Dynamic range can be defined as a ratio between the largest and the smallest detectable wavefront aberration. In interferometry, the basic limit is given by the maximal wavefront slope which causes the frequency of interference fringes to reach the Nyquist limit. Nyquist condition restricts the maximal detectable slope value to $\lambda/2$. Minimal slope value is assumed to be zero, which corresponds to constant intensity over the entire interferogram.

Detection process for S-H sensor is different and the dynamic range strongly depends on accuracy of spot searching algorithms. Common algorithms are averaging the intensity distribution on CCD chip in areas corresponding to subapertures. Maximal measurable wavefront slope causes maximal displacement within the subaperture, which is equal to one half of the microlens diameter

$$W'_{max} = \frac{\Delta x_{max}}{f} = \frac{d_A}{2f}. \quad (3.1)$$

If the position of the spot leaves the restricted area, it cannot be further distinguished from the neighboring spot. Equation 3.1 does not take into account the finite size of the point-spread function, so it has to be corrected for the spot size d_S :

$$W'_{max} = \frac{d_A - d_S}{2f}. \quad (3.2)$$

The spot size is given by equation

$$d_S = \frac{d_A}{2N_F}, \quad (3.3)$$

where

$$N_F = \frac{d_A^2}{4\lambda f} \quad (3.4)$$

is the Fresnel number of an individual subaperture. This equation is only applicable when the spot has a compact shape and is diffraction limited. In reality, spots are broadened by partial

coherence of incoming light or by coma/astigmatism introduced by microlenses for strongly tilted wavefronts. An additional factor c is introduced to describe the differences between the actual and diffraction-limited spot size. Maximal detected wavefront slope for S-H sensor is then

$$W'_{max} = \frac{d_A - cd_S}{2f} = \frac{d_A^2 - 2\lambda fc}{2d_A f}. \quad (3.5)$$

Measurement sensitivity is the minimum slope that the sensor can measure:

$$W'_{min} = \frac{\Delta x_{min}}{f} = \frac{kp}{f}. \quad (3.6)$$

Minimal spot displacement depends on the accuracy of centroid location algorithm, pixel size and the signal-to-noise ratio of the sensor. k is the order of precision of centroid algorithm (for $k=1/100$ pixels the ratio of the spot size to the pixel size exceeds 3.5 [33]).

Dynamic range of S-H sensor can thus be calculated as

$$\frac{W'_{max}}{W'_{min}} = \frac{d_A - cd_S}{2f} = \frac{d_A^2 - 2\lambda fc}{2kpd_A}. \quad (3.7)$$

The factor c describing the actual spot size is very important because it contributes to **cross-talk effect**. The diffraction limited spot has an intensity profile described by $\text{sinc}^2\left(\frac{d_A}{\lambda f}(x - x_S)\right)$, where x_S is the position of the shifted spot. This function shows oscillating side lobe behaviour and might influence the intensity of other spots. Side lobes contributing to the next subaperture cause the shift in centroid position.

3.2 Simulation

Two methods of wavefront detection, phase shifting interferometry and S-H sensor, have both advantages and disadvantages as discussed before. In order to check which one is more suitable for measurement of aspheres, a simulation was carried out in custom written Octave program *Aspherix* (description is in section 4.2). The aspherical wavefront was theoretically measured using ESDI Intellium interferometer and HASO Shack-Hartmann sensor (parameters are listed in Table 3.1 and Table 3.2).

Aspheres have to be tested on interferometer with non-adapted wavefront, since no transmission asphere or compensating element is available. As a fact, there will always be non-zero aspherical component in the detected wavefront. However, the clever selection of radius of the reference sphere can minimize optical path difference (OPD) and increase the chance of correct wavefront reconstruction. Comparing the asphere with this **best fit** sphere will reduce the density of fringes on the detector to the lowest value.

Interferometer	Intellium Z100
Type	Fizeau interferometer
Laser source	He-Ne laser, $\lambda=632.8$ nm, power 1mW
CCD chip resolution	maximal 2048x1536, user can change it to 1024x768 or 512x384
Transmission spheres	F#=0.75 F#=1.5 diameter 100 mm F#=3.3

Software	IntelliWave 6.5
Interferogram analysis method	Phase shifting, 4-step algorithm
Unwrapping algorithm	default Curvature Guided

Table 3.1: Parameters of Intellium interferometer used for theoretical calculations

HASO Shack-Hartmann sensor	
Array size	24 mm
Number of microlenses	160
Focal length	5 mm
CCD chip resolution	3200 pixels
Subaperture diameter	0.15 mm
Pixel size	7.5 μm

Table 3.2: Parameters of S-H sensor used for theoretical calculations

The minimal optical path difference between asphere and reference sphere is used for calculations. Aspherix program calculates optical path difference in normal direction (see Figure 3.1). This wavefront is analyzed by phase shifting method and simultaneously by S-H sensor.

When it is analyzed by phase shifting method, 4 interferograms are acquired after the relative phase shift in the reference wavefront was introduced. Phase resp. wavefront is reconstructed by conventional unwrapping algorithm. When the wavefront slope per pixel exceeds $\lambda/2$, sampling is not sufficient for correct reconstruction. Assuming the ideal conditions, aspherical wavefront is sampled by maximal number of available pixels - 1536.

In the simulation, the same wavefront is also detected by S-H sensor. The beam diameter is adapted to the diameter of a microlens array (it means using a beam reducer in practice). When the marginal spots appear out of detector, the diameter is reduced. The spot positions are found using conventional centroiding algorithm, which fails if the spot shift exceeds the half of microlens aperture. Calculating the factor c of real spot size is a diffraction problem, so in our simplified calculations, we assume it is equal to 1 and the spots are diffraction limited.

Several spot-searching algorithms were designed to correctly assign the spot to its microlens even when the spot left the subaperture area [34, 35]. These algorithms increase the dynamic range of the

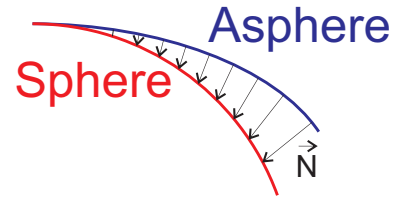


Figure 3.1: Optical path difference between asphere and sphere in normal direction

sensor. If the use of advanced spot-searching algorithm is assumed in the simulation, the detection process is limited by intensity cross-talk. Influence of cross-talk effect is evaluated numerically; it is regarded as significant if it causes the centroid position shift by more than 0.1 pixel. Centroid position is calculated as intensity weighted mean of spot coordinates. The range for the calculation was chosen to be an area as big as one microlens centered at the shifted spot position.

Results

In interferometry, the maximal allowed slope per pixel p_i is

$$\frac{W'_{max}}{p_i} = \frac{\lambda}{2}. \quad (3.8)$$

Shack-Hartmann sensor has maximal detectable wavefront slope per aperture

$$\frac{W'_{max}}{d_A} = \frac{d_A^2 - 2\lambda fc}{2d_A f} = 17.0375 \lambda. \quad (3.9)$$

Simulation was performed for 11 aspheres available in MEOPTA, for their parameters see Appendix A.

Asphere	Intellium interferometer		S-H sensor	
	Max slope per pixel [λ]	Measured	Max slope per subaperture [λ]	Measured
A1	0.3849	Yes	23.785	No
A2	1.9143	No	116.8367	No
A3	0.5766	No	35.0637	No
A4	0.717	No	44.1011	No
A5	0.7077	No	43.3763	No
A6	1.561	No	100.0278	No
A7	0.3185	Yes	19.7349	No
A8	0.2832	Yes	17.6267	No
A9	0.016	Yes	1.0224	Yes
A10	2.042	No	127.6521	No
A11	0.1008	Yes	6.283	Yes

Table 3.3: Comparison of interferometry and S-H sensor for measurement of aspherical wavefronts using classical reconstruction algorithm for S-H

Asphere	Intellium interferometer		S-H sensor	
	Max slope per pixel [λ]	Measured	Max centroid shift [px]	Measured
A1	0.3849	Yes	0.0747	Yes
A2	1.9143	No	0.3701	No
A3	0.5766	No	0.079	Yes
A4	0.717	No	0.0785	Yes
A5	0.7077	No	0.096	Yes
A6	1.561	No	0.0736	Yes
A7	0.3185	Yes	0.1067	No
A8	0.2832	Yes	0.0739	Yes
A9	0.016	Yes	0.0752	Yes
A10	2.042	No	0.1732	No
A11	0.1008	Yes	0.09331	Yes

Table 3.4: Comparison of interferometry and S-H sensor for measurement of aspherical wavefronts using classical reconstruction algorithm for S-H

3.3 Discussion

As the results listed in Table 3.3 indicate, phase shifting interferometry is more efficient method for aspherical wavefront analysis. 5 out of 11 available aspheres can be successfully measured with phase shifting and unwrapping algorithms. Problems are caused by steep wavefront at the edges, where the resolution of detector is not enough to display the fringes without aliasing. With S-H sensor for detection, 9 aspheres cause an average wavefront tilt across one subaperture exceeding the given subaperture area. In other words, many spots are out of detection range of conventional centroiding algorithms.

If advanced centroiding algorithm is used instead, the dynamic range of the sensor is increased. In this case, not only the slope, but also the curvature of the wavefront becomes important. Fast changes in the slope cause an overlap between neighboring spots. Most of the aspherical wavefronts also have the highest curvature close to the edge, so intensity cross talk often changes the centroid position of marginal spots. 8 aspheres can be measured without the cross talk problems.

S-H sensor with advanced centroiding algorithm is the best choice for measurement of aspherical wavefronts. However, this algorithm is not implemented in common S-H sensors, so phase shifting interferometry becomes a preferred method. Not only because it has the higher dynamic range, but also much better spatial resolution. Generally, changes introduced to the wavefront by surface deformations are averaged within one subaperture of S-H sensor. Outcomes of the simulation show that the next work should focus on aspherical wavefront analysis using phase shifting interferometry.

Chapter 4

Non-null Testing

Eliminating the null condition makes testing of aspheres using conventional interferometers difficult. A null condition is a natural consequence in the measurements since the spherical wavefront emerging from transmission sphere can be matched to the test surface. The surface errors are then directly measured in the detector plane. In a non-null configuration, detected optical path difference can be too high to be later correctly interpreted by phase retrieval algorithms. In addition to surface figure information, we need to deal with system aberrations. In Figure 4.1 a), incoming rays retrace themselves and the system aberrations will not affect the OPD. Unfortunately, in case 4.1 b), the different paths of incoming and reflected rays introduce aberrations of interferometric optics. This so called retrace error is further explained in chapter 5.

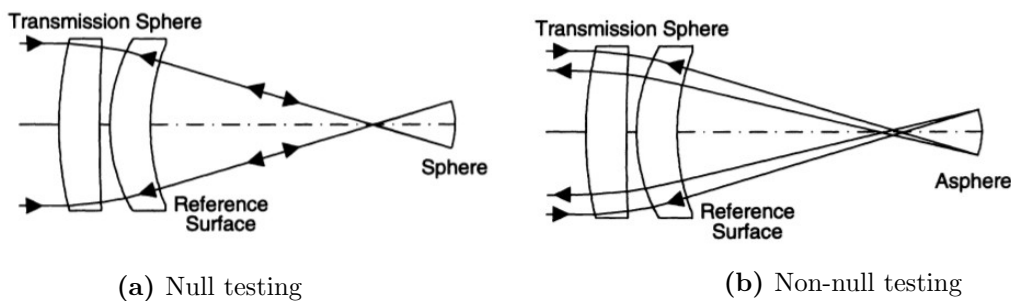


Figure 4.1: Differences between null testing and non-null testing. Replacing a sphere in null setup by an asphere changes the direction of reflected rays. [36]

Despite the problems connected with non-null testing, we decided to use this method for testing of aspheres and verify that it is, in some cases, an easier and better option than null testing. There are several reasons why null testing is avoided in general. First of all, there is no guarantee that it's possible to design a compensating element for testing of desired aspheres. The mainly spherical aberration introduced to wavefront by aspherical optical component can be too high to be compensated by any spherical optics. The uncertainty associated with measurements with null compensator becomes large for steep aspheres, especially when the surface has high numerical aperture. Still, even if the compensating element exists, its design may put too high constraints on alignment

of the system. The null component needs to be fabricated with higher level of precision than all the other elements in the system. In other words, the imperfections of real compensator need to be either negligible or precisely known. The null component is a part of the reference beam, so its deformations or misalignment will add up deformations to the measured surface. Manufacturing a lens or a mirror with tight tolerances is difficult and not cost-effective.

Generally, aspherical lenses differ in shapes and null component usually works only for the aphere it was designed for. The non-null testing is a more universal method. It does not require any auxiliary optics or complicated arrangements.

This chapter describes the concepts and limitations of non-null testing of aspheres and its usage based on experimental results. All measurements were done on Intellium Fizeau interferometer, already available in MEOPTA, which was bought for the purpose of spherical lens testing. Our hypothesis is that non-null testing will work for weak aspheres, though there will be a problem with the strong ones. Theoretical and experimental limits of the interferometer for measurement of aspheres are discussed and compared. For now, we assume that the influence of retrace error on our measurements is negligible. The experiments will show if this assumption is correct and if the non-null testing is a reliable method.

Parameters of Intellium Interferometer

Basic parameters of ESDI Intellium Z100 interferometer are listed below. IntelliWave software performs the wavefront analysis.

Interferometer	ESDI Intellium Z100
Type	Fizeau interferometer
Laser source	He-Ne laser, $\lambda=632.8$ nm, power 1mW
CCD chip resolution	maximal 2048x1536, user can change it to 1024x768 or 512x384
Transmission spheres	F#=0.75 F#=1.5 diameter 100 mm F#=3.3

Software	IntelliWave software
Interferogram analysis method	Phase shifting, 4-step algorithm
Unwrapping algorithm	default Curvature Guided

Table 4.1: Interferometer and software basic parameters important for further calculations

4.1 Measurement Procedure

The following procedure is based on null testing of spheres and is further modified. Since there is no aspherical reference available, the interference fringes observed on the camera represent the

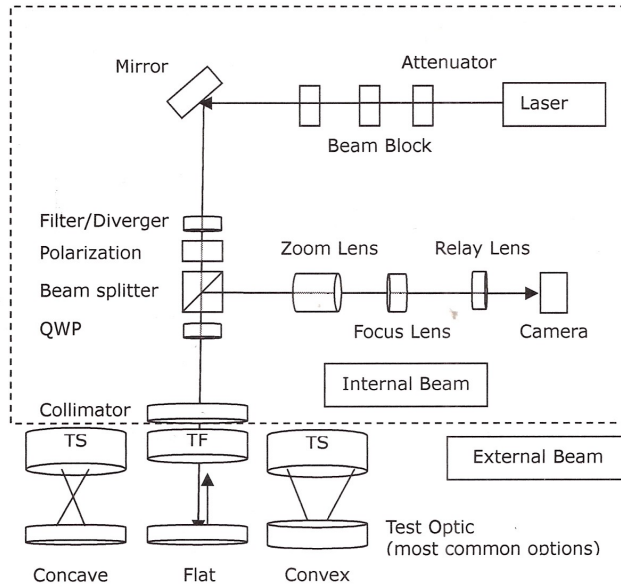


Figure 4.2: Basic scheme of Intellium Fizeau interferometer [37]

optical path difference between reference spherical and real aspherical wavefront. OPD between ideal spherical and ideal aspherical wavefront is theoretically calculated on computer under ideal conditions - perfect alignment and no reference optics aberrations. The predicted value of OPD is subtracted from the measured wavefront. The result represents the OPD between ideal aspherical and real aspherical wavefront (Figure 4.3). Finally, the information about aspherical surface deformations is extracted; the same results as we would obtain in adapted wavefront testing.

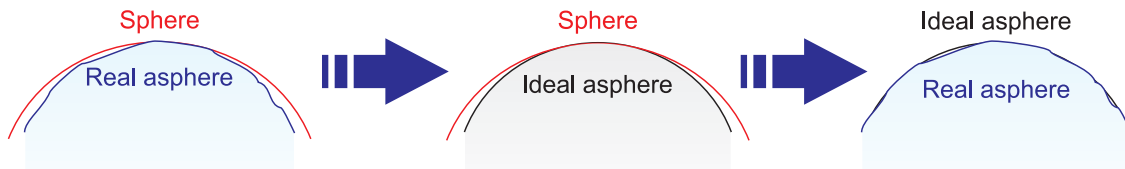


Figure 4.3: Non-null testing process. The OPD between ideal asphere and ideal sphere has to be isolated from measured data.

Optimal conditions for measuring an asphere on Intellium Fizeau interferometer are the output of a computer simulation in custom-written Octave program *Aspherix*. The details about the optics inside Intellium interferometer including the parameters of transmission sphere are unknown; the simulation works only with the asphere and reference surface. For this reason, it cannot produce an exact image of the wavefront on the detector. For now, the retrace errors are ignored, only the test arm of the interferometer is raytraced in *Aspherix*. Influence of retrace error will be discussed in the next chapter. Experimental data are analyzed in *IntelliWave* software, unwrapping the phase from 4 acquired interferograms. The accuracy of non-null testing depends on arranging the same measurement conditions as *Aspherix* program suggests.

Detailed procedure step by step:

1. Parameters of aspherical lens to be tested are inserted to Aspherix program.
The simulation will check if this asphere can be measured using the current transmission spheres available. If it is possible, it will find the best position and corresponding F# of available transmission sphere.
2. The transmission sphere with the most suitable F# is mounted on Intellium interferometer.
3. Asphere is moved to the focal point of the transmission sphere.
Even though the entire surface is aspherical, the reflection from the central part interfering with the reference beam will always create the cat's eye-like interferogram picture. The focal point is a reference coordinate for any future position measurements.
4. Asphere is translated towards the transmission sphere for convex surface or in the opposite direction for concave surface. The value of the translation distance is a key factor in final data interpretation and it is computed by Aspherix program.
When digitizing an interferogram with a detector array, the sampling theorem requires the minimum local fringe spacing to be greater than twice the pixel separation. The wavefront asphericity recorded by detector can be lowered by placing the asphere at correct position. Translation distance defines the radius of the spherical wavefront interfering with the surface reflection. Generally, it is not equal to vertex radius of curvature of the asphere. The radius of so called **best fit sphere** minimizes the deviations between test and reference wavefronts. Best fit radius was computed before in Aspherix.
The reflected beam does not always return to the interferometer having the same diameter as the reference beam. The incident beam might be larger than diameter of asphere, so marginal rays are not reflected at all. Furthermore, rays reaching the asphere do not fulfill the condition of normal incidence, so reflected beam size might vary as it travels. In case the diameter of reflected beam is smaller than the aperture of the transmission sphere, the full resolution of CCD chip is not used. In that case it is possible to apply optical zoom of interferometer optics. If it overfills the aperture, only the fractional part of the surface is displayed on detector.
5. Phase shifting technique is used for OPD reconstruction.
IntelliWave software acquires four interferograms with 90° phase shift in between. The phase (and wavefront shape respectively) are unwrapped using default algorithm.
6. Theoretical OPD calculated in Octave program has a form of rotationally symmetric Zernike coefficients. Computer simulation in Aspherix assumes the ideal conditions, hence anti-symmetric aberrations are zero. In reality, they are always present due to improper alignment of lens and transmission sphere. Symmetric coefficients are entered into IntelliWave software and displayed as theoretical wavefront. Then it is set as a reference wavefront for the following calculations and it is subtracted from the experimental results. The difference describes

aspherical surface deformations as a combination of Zernike polynomials.

4.2 Computer Program for Theoretical Simulations

The program needed for this thesis was written in Octave, high-level interpreted language primarily intended for numerical computations. Its code is published on CD attached. The program runs from the script `Aspherix.m`. `Aspherix` can do ray tracing of interferometer test arm, wavefront shape calculations and optimization of the current interferometer setup. It was written to be interactive; it requests the user to type the parameters of an asphere and offers the best options for the Intellium interferometer configuration. It also visualizes the lens testing process free from alignment and system errors.

Program input

I Parameters of tested surface, as written on optical drawing

Rotationally symmetric aspherical surface z_a is described by equation

$$z_a = \frac{\frac{1}{ra} \cdot r^2}{1 + \sqrt{1 - (K + 1) \frac{1}{ra}^2 \cdot r^2}} + \sum_{i=1}^4 A_i \cdot r^{2i} \quad (4.1)$$

as a function of radial coordinate r . The required parameters for the program are the surface orientation (convex/concave), vertex radius of curvature ra , optical diameter of the lens, conic constant K , coefficients of asphericity A_i .

The user can pick up the asphere from a list (details of all currently available aspherical lenses in MEOPTA are also written in Appendix A) or enter the parameters of sphere/asphere manually. Sag table immediately appears and the values have to be confirmed or there is a chance to correct the previous input.

I Position of the asphere with respect to the focal point of transmission sphere

Radius of the best fit sphere is already calculated for 11 available aspheres. Asphere can be moved to best fit position or by user defined value. The best fit sphere radius can be later calculated if requested.

I Number of rays to display

The entire system is raytraced with 1500 rays, but the number of rays to display is limited to 50 rays as plotting the graphics might slow down other computations.

I Transmission sphere F#

Possible choices are F# 0.75, 1.5 and 3.3. The best one is always suggested beforehand.

Program output

O Diameter of the asphere illuminated by chosen transmission sphere

It is possible that none of the available transmission spheres is sufficient to illuminate the entire aspherical surface. The program informs how much of the asphere is actually/certainly measured..

O Reflected beam diameter, number of pixels used for calculations

Reflected beam diameter influences the calculations in two ways: it either decreases the camera resolution or results in displaying an incomplete image of the tested surface. An example is shown in Figure 4.4. In Figure 4.4 (a), asphere A10 is measured in the best fit position. Since the reflected beam d_r is approximately half of the transmission sphere diameter, an interferogram will be sampled only by $d_r/D_{obj} \cdot 1536$ pixels. The program uses 1536 as the maximal resolution of the chip. If the reflected beam is cut by the aperture of transmission sphere, it means that marginal parts, where the ray deviation is the highest, are not visible on the detector. When asphere A10 is translated 34 cm further from the best fit position, reflected beam diameter exceeds D_{obj} . Imaged diameter of the asphere is then $D_{obj}/d_r \cdot d$; assuming d is the full diameter.

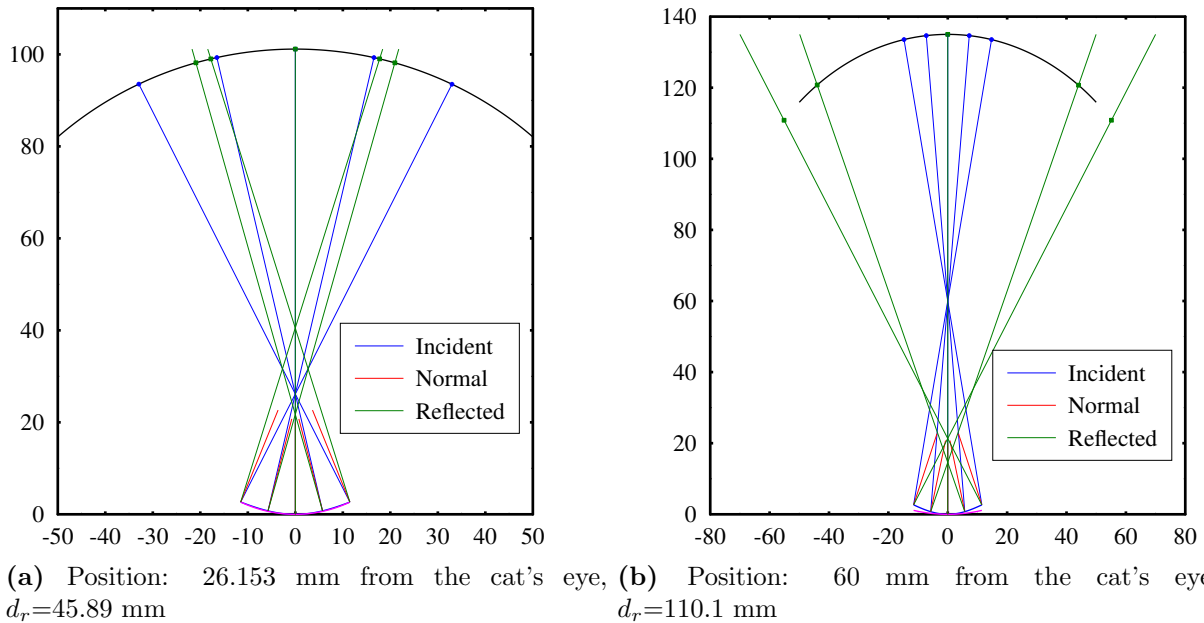


Figure 4.4: Influence of the reflected beam diameter on non-null testing parameters. In case (a), reflected beam is imaged on 705 pixels. In case (b), \varnothing 20.89 mm is displayed, full diameter $d=23$ mm.

O Optical path difference

The last surface of transmission sphere which serves as a reference is concentric with the spherical reference wavefront. It has the diameter D_{obj} and radius of curvature $D_{obj} \cdot F\#$.

The OPD is calculated in two ways: a) with respect to the reference surface after ray tracing, b) normal direction difference (Figure 4.5). Both values coincide only when all rays reach

asphere in normal direction.

OPD is characterized by statistical parameters Peak-to-valley (PV) and Root mean square (RMS):

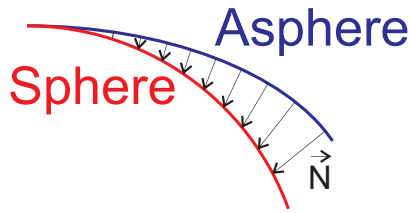


Figure 4.5: OPD in the normal direction

$$PV = \max(OPD) - \min(OPD) \quad (4.2)$$

$$RMS = \sqrt{\text{mean}(OPD)^2 + \text{std}(OPD)^2}. \quad (4.3)$$

○ Zernike coefficients

OPD wavefront is decomposed into rotationally symmetrical Zernike polynomials. The program calculates symmetrical coefficients with numbers 1, 4, 9, 16, 25, and 36 (see Appendix B), non-symmetrical coefficients are equal to zero.

○ F# of the best transmission sphere

Transmission sphere minimizing the angle of incident rays is suggested by the program.

○ Best measurement configurations

The output is the combination of F# and position where the reflected beam diameter is less than diameter of reference surface. In the same time, the sampling on CCD chip is sufficient to correctly capture the cosine modulation of the OPD wavefront. In other words, the Nyquist condition is valid everywhere and we can successfully measure entire diameter of the asphere. Program shows the distance range for given transmission sphere where the best results are obtained.

○ Figure: The layout

The layout shows the test arm of Fizeau interferometer: the asphere, the fitting sphere, the reference surface of the transmission sphere, chosen number of traced rays.

○ Figure: Interferogram

OPD is shown as an interferogram.

○ Figure: Angle of incidence on tested surface

Graph shows how far are the rays from normal incidence on in each part of the asphere.

○ Figure: Ray height difference on the reference surface

Graph displays how far is the path or reflected rays from incident ones.

○ Figure: Wavefront slope

According to Nyquist condition, the wavefront can be correctly reconstructed if the slope per one pixel on detector does not exceed $\lambda/2$. The threshold values are also shown for comparison.

Figure: OPD with areas where Nyquist condition is not violated

The regions where the reconstruction is possible are highlighted.

4.3 Theoretical Limits of Intellium Interferometer

The slope of the aspherical wavefront, which can be measured on the interferometer is related to the detector chip resolution. We will make a simplified assumption that OPD can be described by $z_a = A_2r^2 + A_4r^4$, neglecting the higher coefficients of asphericity. For most of the aspheres, the term A_4 is dominant. The quadratic term in the equation can be changed by varying the distance from the focal point and it is minimized in the best fit position. The biggest aspherical departure from the sphere z_m is not necessarily on the edge; actually, we do not want the maximum to be on the edge. In order to find the best fit sphere, the slope on the edge should be equal to the slope in position r_0 with the opposite sign (Figure 4.6).

Asphere, its slope and curvature can be written as

$$z_a = A_2r^2 + A_4r^4 \quad (4.4)$$

$$s = \frac{dz_a}{dr} = 2A_2r + 4A_4r^3 \quad (4.5)$$

$$c = \frac{d^2z_a}{dr^2} = 2A_2 + 12A_4r^2. \quad (4.6)$$

The condition for maximal slope is

$$2A_2r_m + 4A_4r_m^3 = -s_m \quad (4.7)$$

$$2A_2r_0 + 4A_4r_0^3 = s_m. \quad (4.8)$$

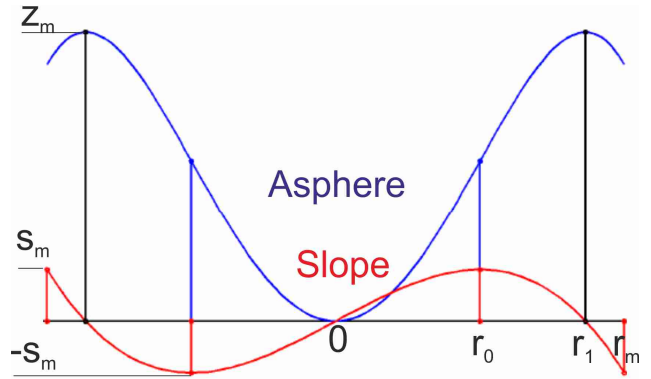


Figure 4.6: Aspherical wavefront in the best fit position

For coordinate r_0 with the maximal slope the curvature is zero

$$2A_2 + 12A_4r_0^2 = 0. \quad (4.9)$$

Coordinate r_1 with the maximal aspherical departure has zero slope:

$$A_2r_1^2 + A_4r_1^4 = z_m \quad (4.10)$$

$$2A_2r_1 + 4A_4r_1^3 = 0. \quad (4.11)$$

From (4.7) -(4.11), we get the unknown values of coefficients and coordinates as a function of z_m

and r_m [38]:

$$\begin{aligned}
A_2 &= \frac{8z_m}{3r_m^2}; & A_4 &= -\frac{16z_m}{9r_m^4} \\
r_0 &= \frac{r_m}{2}; & r_1 &= \frac{\sqrt{3}r_m}{2} \\
s_m &= \frac{16z_m}{9r_m}
\end{aligned} \tag{4.12}$$

If this aperture is imaged on the detector with p pixels, the maximal wavefront difference per pixel is related to maximal slope and radial coordinate difference per pixel Δr

$$\Delta z = s_m \Delta r = \frac{16z_m}{9r_m} \frac{2r_m}{p} = \frac{32z_m}{9p}. \tag{4.13}$$

Since Fizeau interferometer is the double pass system, we should consider maximal aspherical wavefront twice Δz value for further calculations. According to the Nyquist condition, the fringes can be correctly resolved if the maximal wavefront change per pixel is less than $\lambda/2$:

$$\Delta w = \frac{64z_m}{9p} \leq \frac{\lambda}{2} \implies z_m = \frac{9p\lambda}{128} \implies |A_{4m}| = \frac{16z_m}{9r_m^4} = \frac{144}{1152} \frac{p\lambda}{r_m^4} \tag{4.14}$$

A_{4m} is the maximal asphericity of aspherical wavefront which is still resolvable on the detector. With chip of resolution 1536x2048, Table 4.2 compares the real A_4 coefficient to the theoretical one ($p=1536$). In the beginning, we assumed that other coefficients than A_4 are zero. Deriving the expressions for other coefficients would mean solving the system of nonlinear equations, so we used Aspherix to calculate OPD numerically.

Asphere	Optical diameter $2r_m$	A_4	A_{4m}	Measurable
A1	11.4	8.95734e-5	1.15e-4	Yes
A2	22.8	-1.165537e-5	7.19e-6	No
A3	23	-6.760244e-6	6.95e-6	No
A4	22	-4.841939e-6	8.3e-6	No
A5	13.6	-4.076374e-5	5.68e-5	No
A6	16.6	-2.02409e-4	2.56e-5	No
A7	11.4	-3.0574139e-5	1.15e-4	Yes
A8	28.9	-1.16455137e-6	2.79e-6	Yes
A9	35	-2.6934596e-7	1.45e-6	Yes
A10	23	4.13e-5	6.95e-6	No
A11	35	-2.972e-7	1.45e-6	Yes

Table 4.2: Maximal allowed coefficient of asphericity for resolvable fringes in the best fit position

In theory, around half of the aspheres (5 of 11) can be measured on Intellium interferometer in the best fit position when the full resolution is used. However, aspherical wavefront changes its shape and ideal condition, when the full resolution of detector is used, is almost never true.

4.4 Comparison of Unwrapping Algorithms

IntelliWave software allows the user to choose an algorithm for phase-unwrapping. Conventional as well as Sub-Nyquist algorithms are the supported options. Conventional algorithms include Branch Cut Minimization (BCM), Tiled Modulation Guided, Curvature Guided, Preconditioned Conjugate Gradient and Minimum Discontinuity. BCM algorithm is the fastest solution, but it usually fails with noisy data. Other algorithms are more complex, they can deal with extremely noisy data, but require more computational time. There are 3 types of Sub-Nyquist algorithms available: Path Dependent, Path Independent 1, Path Independent 2.

Two experiments were carried out to determine the efficiency of unwrapping algorithms under different conditions. The first experiment was a test of Sub-Nyquist unwrapping algorithms. In the second one, we evaluated how are the algorithms affected by noise in the data.

IntelliWave has a feature which allows to display theoretical wavefront when the Zernike coefficients are known. In one experiment, wavefront with spherical aberration of 30λ was generated in IntelliWave. With the lowest possible resolution of the camera (384×512 pixels), it is clear that the slope cause discontinuities in unwrapped phase. It was confirmed by generating interferograms affected by aliasing. Afterwards, classical and Sub-Nyquist algorithms were applied for phase reconstruction using the interferogram data and the result is shown in Figure 4.7.

A scratched spherical lens was chosen as a source of noisy data for the other experiment. Figure 4.8 shows how the noise propagates in unwrapped phase.

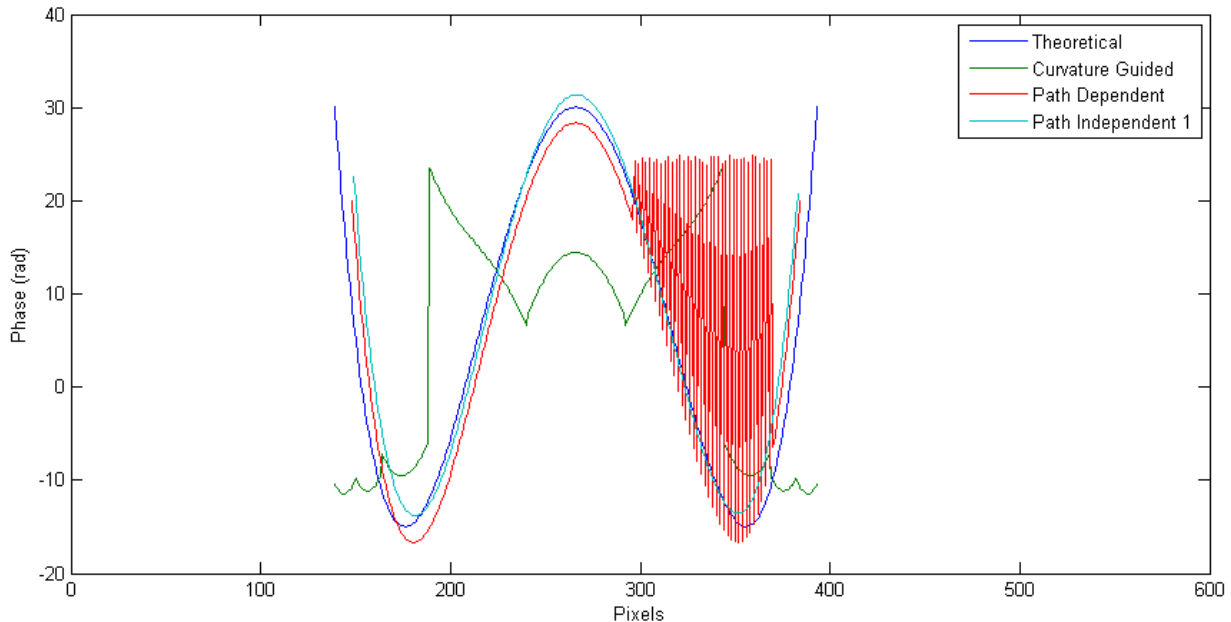


Figure 4.7: Comparison of classical and Sub-Nyquist algorithms for a wavefront reconstruction. Algorithms were applied to reconstruct theoretical wavefront with 30λ of primary spherical aberration.

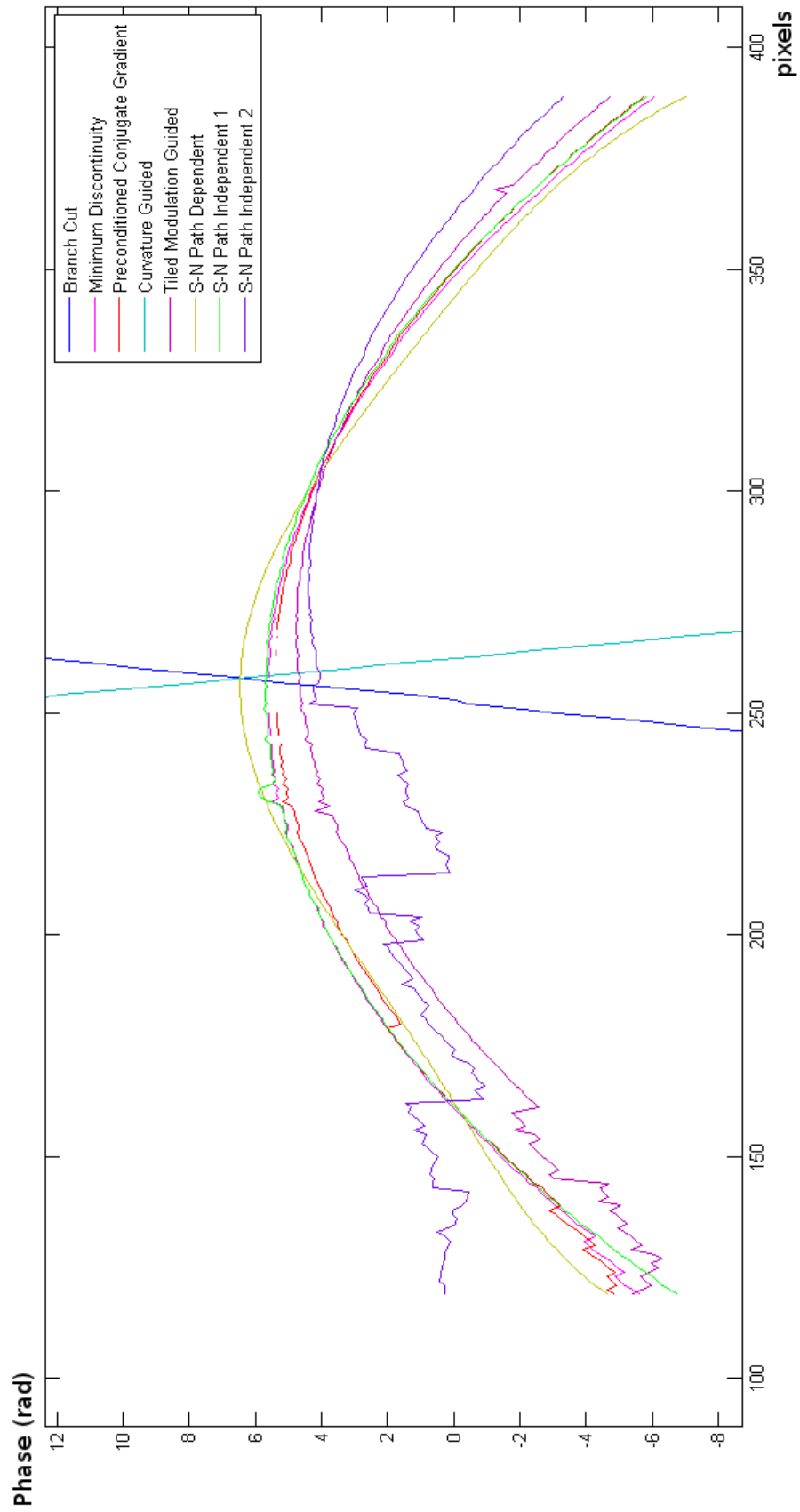


Figure 4.8: Comparison of conventional and Sub-Nyquist algorithms for noisy data reconstruction

Figure 4.7 proves that Sub-Nyquist algorithms work quite well even without the proper hardware (pinhole mask). As expected, classical Curvature Guided algorithm failed because the Nyquist condition is violated. Sub-Nyquist Path Dependent algorithm cannot properly deal with noisy data and the errors are spread over the wavefront points reconstructed later (see oscillations on the right side). Path Independent 1 algorithm gives the most accurate and smooth wavefront reconstruction. How different unwrapping algorithms deal with noisy data is shown in Figure 4.8. Branch Cut and Curvature Guided algorithms totally failed, the reconstructed wavefront resembles tilted plane instead of defocused sphere. Tiled Modulation Gradient scans the interferogram for the correct place to start unwrapping, processes the good data first and then it correctly connects unwrapped regions. In the end, the noisy data are processed to stop the errors from propagating. However, together with Preconditioned Conjugate Gradient algorithm, it does not work well in the region of noisy data (left side of the wavefront). The best conventional algorithm for unwrapping noisy data is Minimum Discontinuity which attempts to minimize all phase discontinuities caused by random noise. According to IntelliWave manual [39], S-N Path Independent 2 algorithm uses polynomials for surface interpolation, so the result should be smooth with high spatial frequencies removed. This fact does not correspond to experimental results. Surface shape, which was found using S-N Path Dependent algorithm, is incorrectly evaluated as concave in the region of noisy data. S-N Path Independent 1 gives the result which visually approaches the expected spherical shape. To sum up the results, the best unwrapping option for the noisy data is to use Minimum Discontinuity algorithm. For data with less noise, there is no significant difference between conventional algorithms in terms of computational time or accuracy of reconstruction. According to the previous examples, we recommend using S-N Path Independent 1 algorithm for unwrapping wavefronts violating Nyquist condition.

4.5 Experimental Verification of Nyquist Condition

A simple experiment was done to check limiting slope value for correct reconstruction with conventional unwrapping algorithms. Sphere with radius of curvature $r=189.23$ mm was defocused from the null position until the discontinuities in unwrapped phase were observed in the image reconstructed by IntelliWave. The same measurement conditions were entered into Aspherix program, the test arm of Intellium interferometer was raytraced. Calculated wavefront slope at the edge of aperture should, according to the experiment, violate the Nyquist condition.

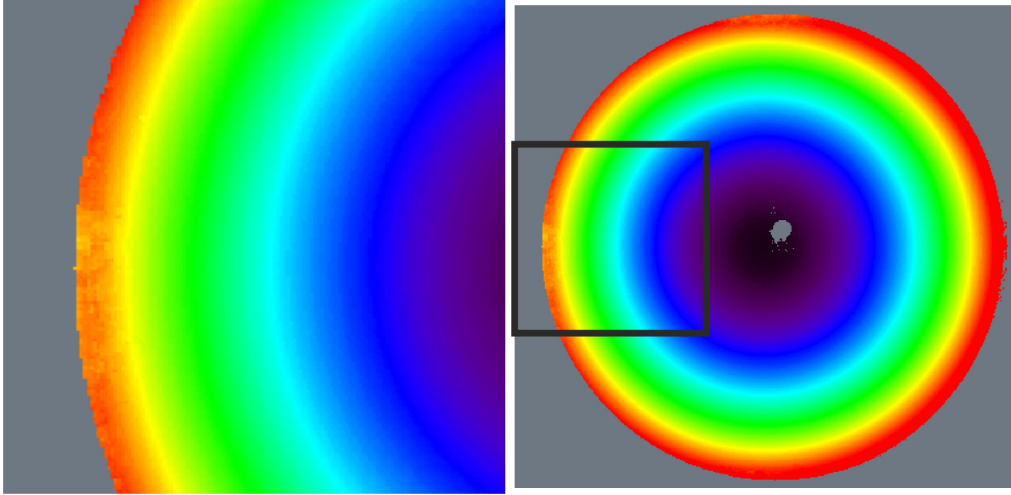


Figure 4.9: IntelliWave phase image for sphere defocused 1.33 mm from the null position

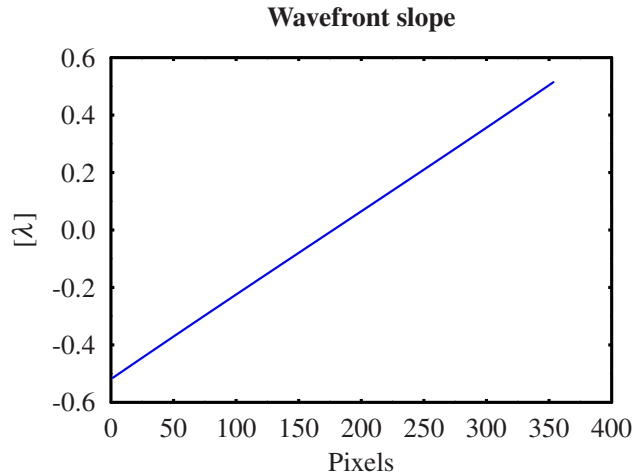


Figure 4.10: Aspherix output: wavefront slope per pixel

The incorrectly unwrapped regions in the image started to be visible for 1.33 mm displacement from the null position. Corresponding maximal slope from Aspherix program is 0.5161λ , which confirms the violation of Nyquist condition. $\lambda/2$ can be still kept as a limit for further calculations.

4.6 Non-null Testing Results

Multiple simulations were carried out in Aspherix program to select the aspheres which can be measured on Intellium interferometer. Two aspheres out of eleven produce reflected wavefront not violating Nyquist condition - LENS 7 and Ge lens.

LENS 7

LENS 7, with the lowest coefficient of asphericity, was the first candidate for non-null testing experiments. The same piece of aspherical lens was also measured on Aspheric stitching interferometer in company Asphericon, so the results can be later compared. Asphericon sent a screenshot (see Appendix C) from MetroPro[®] software.

Best F#	3.3
Best fit position	134.78 mm
Reflected beam diameter	85.552 mm
Pixels	1315
OPD (normal direction)	PV=3.3215 λ , RMS=1.1556 λ
OPD (ray tracing)	PV=3.3215 λ , RMS=1.1539 λ
Measured diameter	35/35 mm
Measurement range	3.3: 129.2-140 mm

Table 4.3: LENS 7: Output from Aspherix program

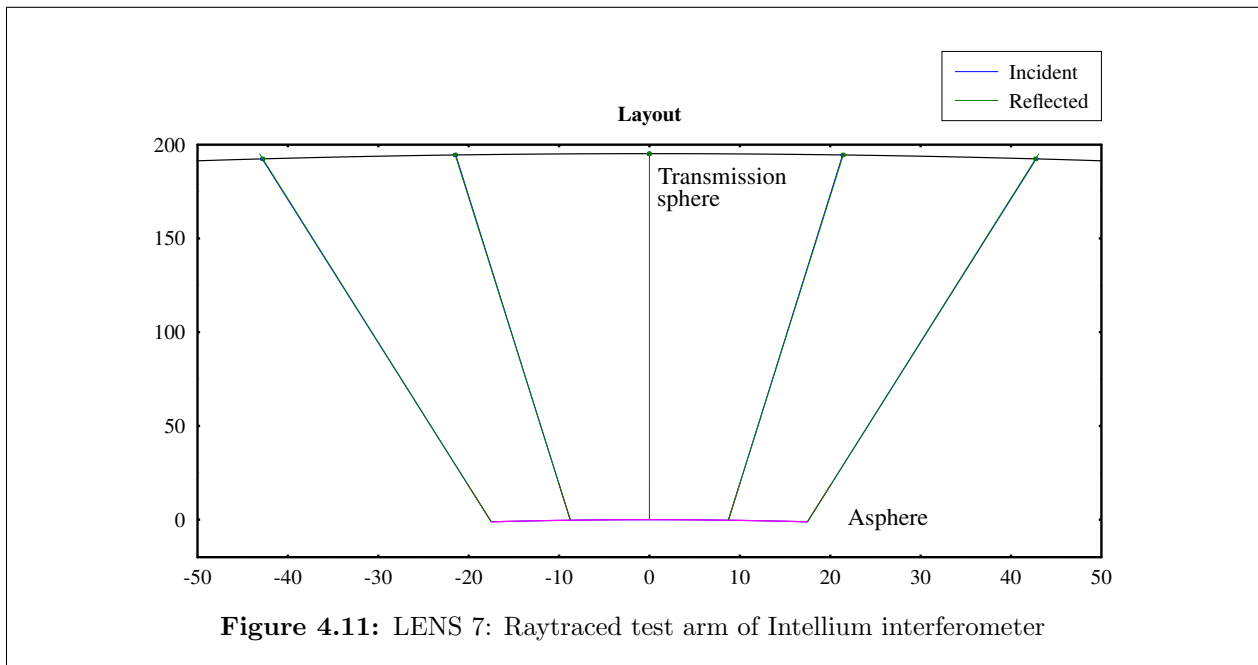


Figure 4.11: LENS 7: Raytraced test arm of Intellium interferometer

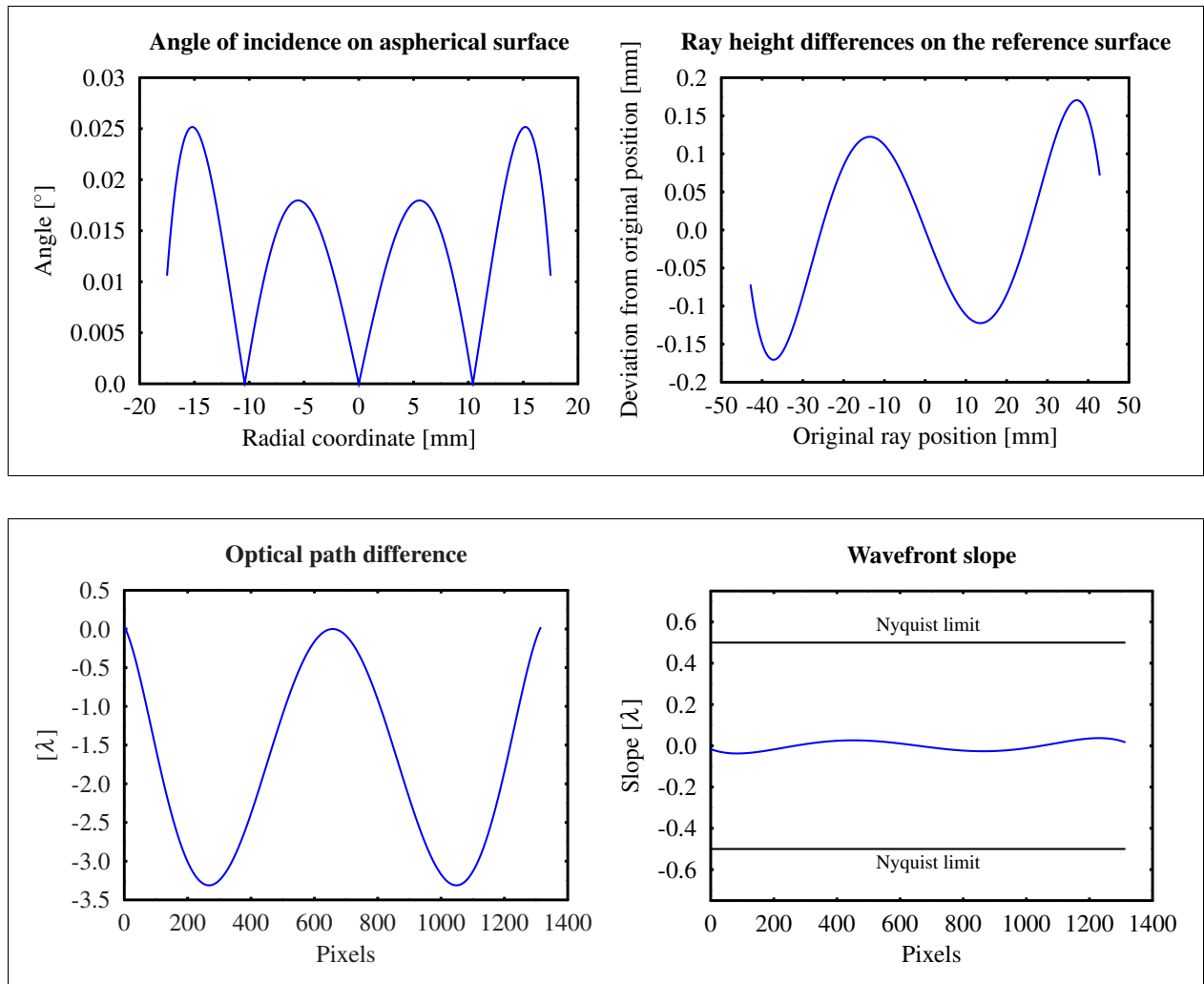


Figure 4.12: LENS 7: Graphical output from Aspherix program

Zernike coefficient	units: λ (623.8 nm)		
	IntelliWave	Aspherix	Difference
1	-0.0011	-1.9814	-0.0011
2	-0.0004	0	-0.0004
3	0.0018	0	0.0018
4	0.8168	0.9199	-0.1031
5	0.0189	0	0.0189
6	0.0270	0	0.0270
7	-0.0044	0	-0.0044
8	-0.0449	0	-0.0449
9	1.9675	1.9669	0.0006
10	0.0132	0	0.0132
11	0.0270	0	0.0270
12	0.0100	0	0.0100
13	-0.0186	0	-0.0186
14	-0.0349	0	-0.0349
15	-0.0528	0	-0.0528
16	-0.9174	-0.9140	-0.0034
17	0.0027	0	0.0027
18	0.0040	0	0.0040
19	0.0072	0	0.0072
20	0.0048	0	0.0048
21	-0.0259	0	-0.0259
22	-0.0113	0	-0.0113
23	-0.0303	0	-0.0303
24	0.0573	0	0.0573
25	0.0432	0.0123	0.0309
26	-0.0031	0	-0.0031
27	-0.0106	0	-0.0106
28	0.0036	0	0.0036
29	0.0004	0	0.0004
30	-0.0174	0	-0.0174
31	0.0016	0	0.0016
32	-0.0113	0	-0.0113
33	-0.0167	0	-0.0167
34	0.0273	0	0.0273
35	-0.0129	0	-0.0129
36	-0.0336	-0.0081	-0.0255

Table 4.13: LENS 7: Surface deformations in form of Zernike coefficients

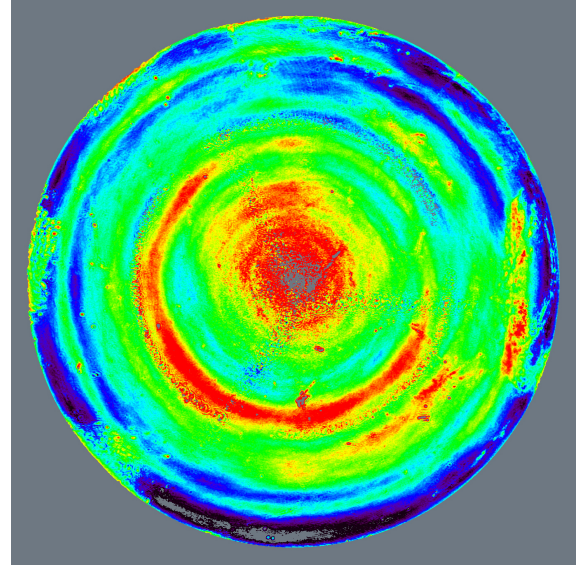


Figure 4.14: LENS 7: Surface deformations measured in MEOPTA

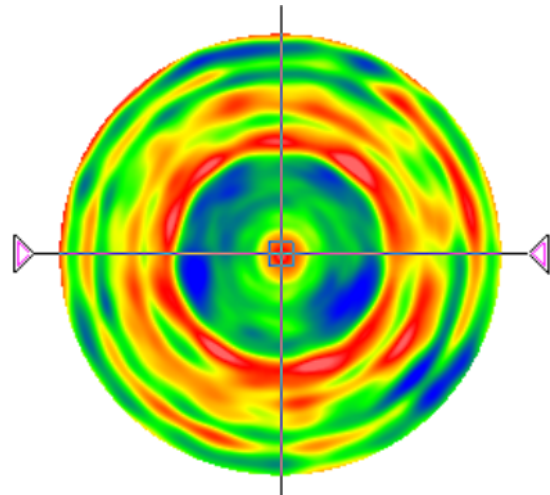


Figure 4.15: LENS 7: Surface deformations measured in Asphericon

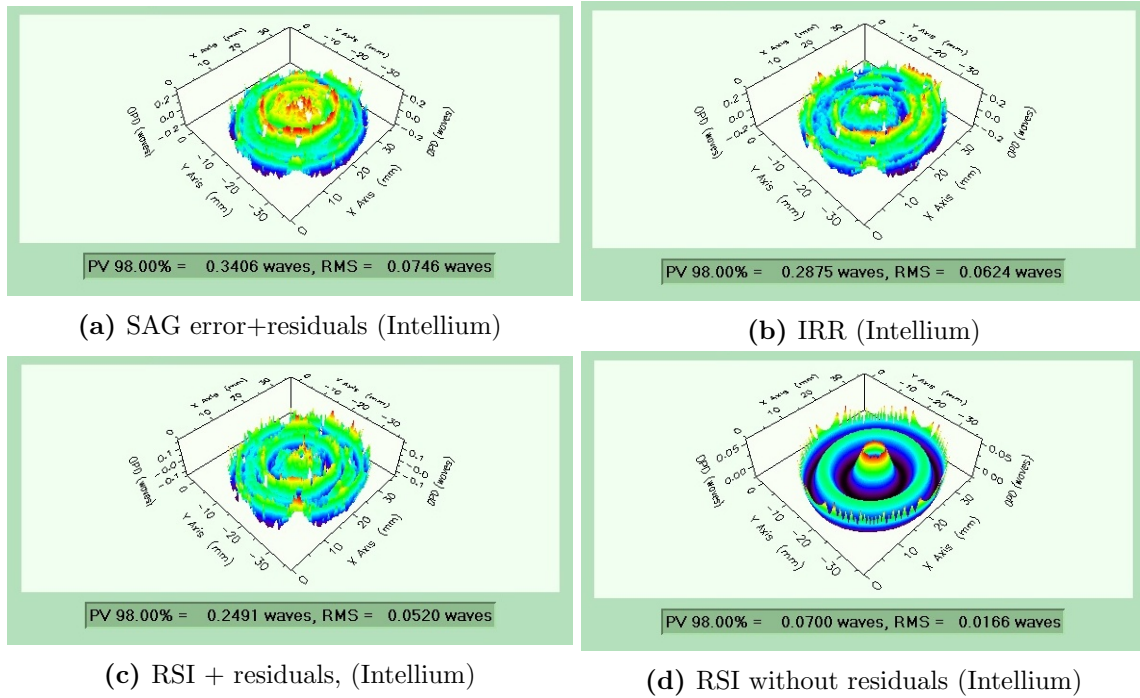


Figure 4.16: LENS 7: Standard deformation errors

Tolerance for aspherical surface deformations is prescribed in an optical drawing of the lens. According to the technical standards, deformations are represented by three errors:

SAG

SAG(Saggita error): The tolerance on power of the surface (4th Zernike coefficient) with respect to the reference sphere.

IRR

IRR (Irregularity): The tolerance on the surface form error which remains after the saggita error has been removed, the PV with respect to the best fit reference sphere.

RSI

RSI (Rotationally symmetric irregularity): The tolerance on the rotationally symmetric component of the surface form error after the best fit sphere has been subtracted.

	Units: $\lambda=632.8$ nm		
	Asphericon	MEOPTA	Drawing tolerance
SAG PV	0.5694	0.3406	1.726
IRR PV	0.3409	0.2875	0.4315
RMS _i	0.0475	0.0624	0.3452
RSI	0.0863	0.2491	0.2589
RSI-residuals		0.07	

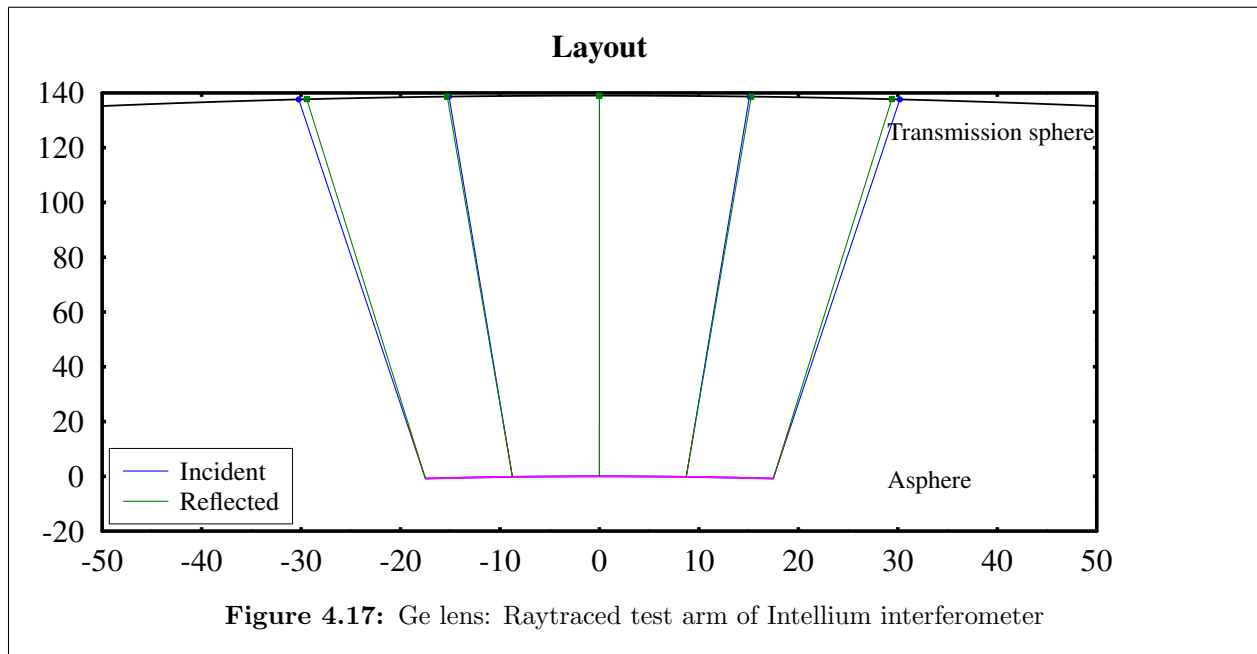
Table 4.4: LENS 7: Surface errors compared to optical drawing

Values available from Asphericon are expressed in fringes of $\lambda=546.07$ nm, but Intellium interferometer works with $\lambda=632.8$ nm. Asphericon values were recalculated for chosen common units - $\lambda=632.8$ nm.

Ge lens

Best F#	3.3
Best fit position	191.1 mm
Reflected beam diameter	58.849 mm
Pixels	904
OPD (normal direction)	PV=10.5801 λ , RMS=3.3646 λ
OPD (ray tracing)	PV=9.5301 λ , RMS=3.3135 λ
Measured diameter	35/35 mm
Measurement range	3.3: 188.4-202.4 mm

Table 4.5: Ge lens: Output from Aspherix program



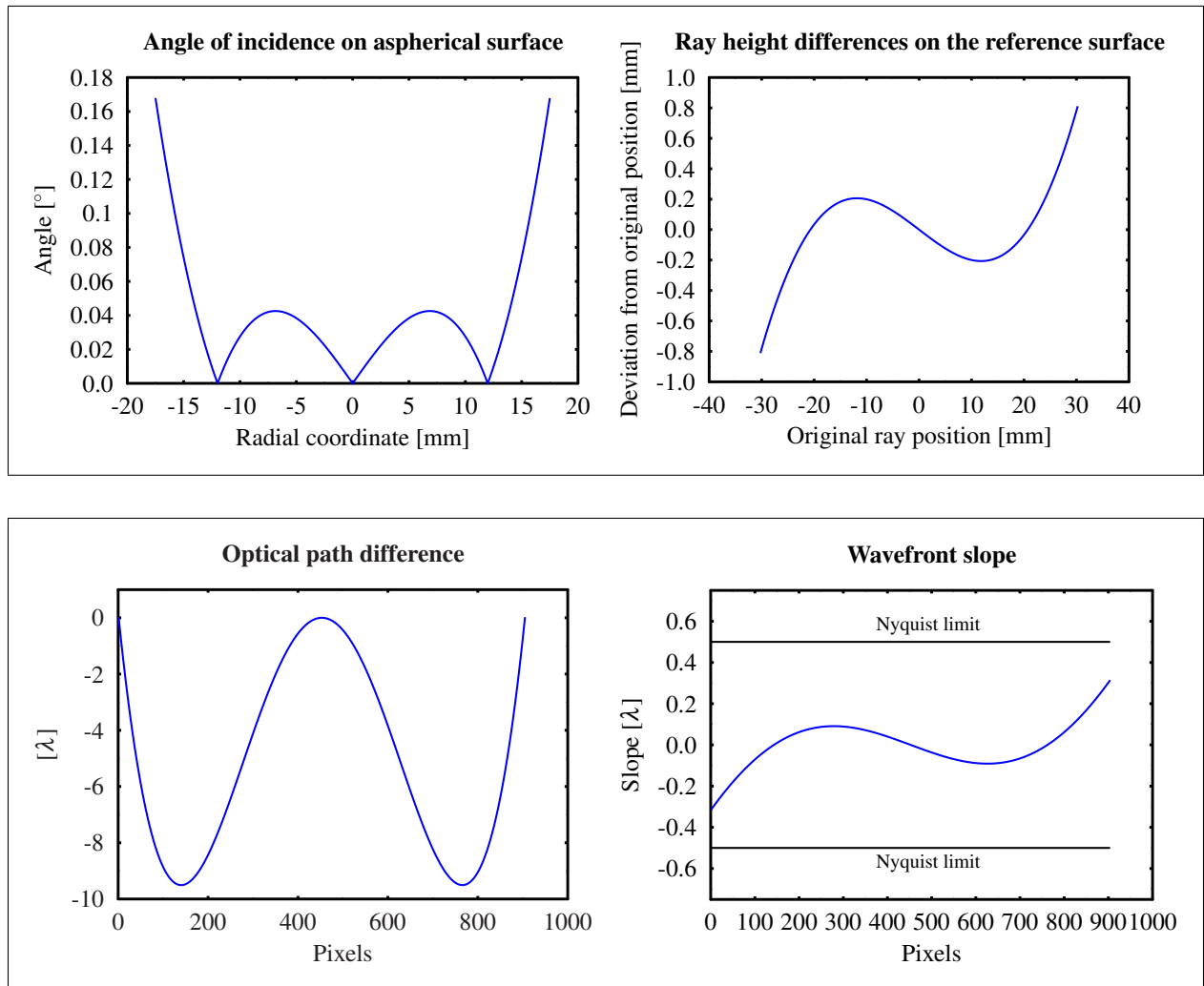


Figure 4.18: Ge lens: Graphical output from Aspherix program

Zernike coefficient	units: λ (623.8 nm)		
	IntelliWave	Aspherix	Difference
1	0.1318	-6.32852	0.1318
2	-0.0000	0	0
3	0.0000	0	0
4	-3.2057	0.33153	-3.5372
5	-0.0090	0	-0.009
6	0.0419	0	0.0419
7	-0.5481	0	-0.5481
8	-0.7643	0	-0.7643
9	4.2365	6.32882	-2.0923
10	-0.0019	0	-0.0019
11	-0.0122	0	-0.0122
12	0.0188	0	0.0188
13	-0.0010	0	-0.0010
14	-0.1000	0	-0.1000
15	-0.1150	0	-0.1150
16	0.4360	-0.31917	0.7552
17	0.0048	0	0.0048
18	-0.0135	0	-0.0135
19	-0.0018	0	-0.0018
20	0.0058	0	0.0058
21	0.0032	0	0.0032
22	0.0260	0	0.0260
23	-0.0322	0	-0.0322
24	-0.0212	0	-0.0212
25	0.1079	0.01186	0.096
26	-0.0020	0	-0.0020
27	0.0012	0	0.0012
28	0.0014	0	0.0014
29	-0.0058	0	-0.0058
30	0.0180	0	0.0180
31	0.0093	0	0.0093
32	-0.0070	0	-0.0070
33	-0.0017	0	-0.0017
34	-0.0308	0	-0.0308
35	-0.0160	0	-0.0160
36	0.0088	-0.00021	0.009

Table 4.19: Ge lens: Surface deformations in form of Zernike coefficients

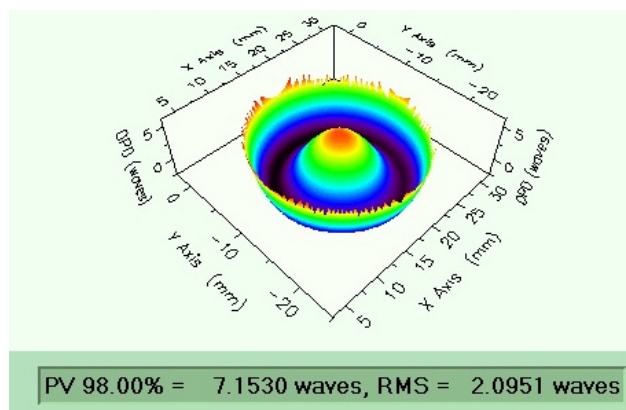


Figure 4.20: Ge lens: Wavefront measured on Intellium

4.7 Discussion

As Figure 4.14 and Figure 4.15 indicate, asphere LENS 7 was successfully measured with proposed non-null testing method. In general, the results on surface tolerances from MEOPTA and Asphericon in Table 4.4 do not differ by more than 0.2λ . The considerable difference in case of Rotationally symmetric irregularity can be explained by the number of Zernike polynomials used for calculating RSI. In Asphericon, RSI PV was probably calculated only from the first four rotationally symmetrical terms. In order to check this, fit residuals were subtracted from the reconstructed OPD and displayed RSI value became a sum of first four polynomials. Both RSI errors are only 0.01λ different. However, when describing surface deformations, it is not reasonable to restrict the number of used Zernike polynomials to standard 36 polynomials. Our previous experience in optical testing suggests that most of the surface deformations can be described by higher order rotationally symmetric Zernike coefficients. Because of this fact, IRR and RSI should have similar values, which was confirmed in the measurement.

Visually comparing surface deformations, both have the same looking central part surrounded by four annular lower valued zones. Although PVs are slightly different, the structure of the surfaces is similar.

To sum up, interferometric measurements revealed that this asphere was manufactured correctly; none of the errors exceeds the value allowed in the drawing. LENS 7 can be measured on Intellium Fizeau interferometer in MEOPTA even without any additional hardware optimized for measurements of aspheres.

On the other hand, non-null measurements of Ge lens show a mismatch between theoretical prediction and experimental data. For example, there is still 2λ in primary spherical aberration which was supposed to be subtracted from the measurement. Such high value means that measurements are influenced by factors which were not previously considered. In case of LENS 7, the unknown error is not significant to the measurement; the accuracy of results is comparable to the accuracy of stitching interferometer. Non-null testing method described in this chapter is simplified by neglecting the influence of retrace error, hence it is probably the cause of problems in Ge lens measurement. In further research, instead of measuring more aspheres, we decided to focus on explanation how retrace error can change the non-null testing results.

Chapter 5

Retrace Error

Creating a reference wavefront that matches the test surface is a goal in the interferometric null tests. If the null condition is met, both test and reference beam follow the common path through the interferometer optics. Null tests are normally implemented to test spherical optics, since the accurate reference objective can produce an almost perfect spherical wavefront. Measurement inaccuracy that results from failure to meet null condition is commonly referred to as **retrace error**. Retrace error will always be present if a sphere is replaced by an asphere while having the spherical reference wave.

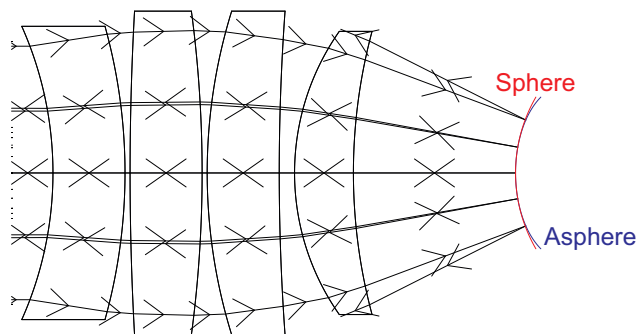


Figure 5.1: Non-null testing of an asphere; incident and reflected rays have the different paths

We recognize two types of retrace error: retrace path error and retrace surface error [40]. Retrace path error is caused by test ray following the different path than reference ray. It is no longer possible to image the point source on itself, thus the aberrations of the interferometer system do not cancel out like they do when rays follow the same path. Moreover, the surface under test is not manufactured perfectly; its deformation will further change the path of incident rays and cause what we call retrace surface error. This error is unpredictable, so we can only assume it is negligible when the surface is well manufactured.

One of the first papers on this topic was published in 1992 [41]. The large spherical aberration of one lens from Hubble space telescope was double checked using different interferometers. The authors noticed an unexpected increase in spherical aberration after displacing the test lens from the null position. The initial reason to move the Hubble lens was to stop overfilling the reference mirror aperture.

An article by Kreischer [42] written from the point of view of optical designer studies the retrace

error as a function of transmission sphere design. Retrace error with regard to testing nominally spherical surfaces is largely ignored, but its influence can be significant when high test accuracy is needed. Author identifies two types of retrace error: Axial; induced spherical aberration resulting from defocus, and Transverse; induced coma as a result of tilt. Both of them were taken into account while designing a new transmission sphere. As results suggest, lower F#, the higher the retrace error. All Kreischer optics transmission spheres were adequately corrected to minimize the effect of retrace error.

In the previous chapter, we present the results of non-null measurement of aspheres using Fizeau interferometer. As comparison with stitching interferometer shows, we were successful in case of LENS 7, however, measurement of Ge lens raised a question about the influence of retrace error. This chapter will study the retrace error and give an explanation why the retrace error plays an important role in data analysis from non-null measurements. The possibilities of removing retrace error will be suggested based on experimental and theoretical results.

Experimental approach was used for retrace error evaluation on Intellium Fizeau Z100 interferometer. Since the manufacturer refused to reveal parameters of transmission spheres or inner lenses, comparison with theoretical predictions was not possible. It was obvious we would receive a negative reply; ESDI company also sells special Fizeau interferometer Intellium Asphere intended for testing of aspheres. Its parameters do not differ from the Z100 model, it even has two transmission spheres $\varnothing 100$ mm with F#s 0.75 and 1.5 included. The newer version of IntelliWave software can compensate for retrace error and the dynamic range of the interferometer is increased by using Sub-Nyquist algorithm.

Behavior of retrace error for aspheres was estimated using the simulation with sphere. Sphere with radius of curvature $r=19.768$ mm was defocused from the best fit position and retrace error was calculated.

The retrace error can be also influenced by using built-in optical zoom, which makes the change in the interferometer setup. Results for Ge lens with and without zoom are compared.

Alongside, theoretical calculations were done on brand new Twyman-Green interferometer, completely designed in MEOPTA. The custom-made components meet all the standards for optical testing. This time, the reference surface is not spherical, but a plane mirror which is much easier to manufacture. Up to the present time, this interferometer is not constructed, but we benefited from the knowledge of the nominal design and checked the options for testing of aspheres. With a full prescription of the system, retrace error for aspheres could be precisely analyzed in lens design software.

5.1 Experimental Approach

The origin of retrace error was already explained, so the important issue to solve was how to quantify it. It was done by comparing the changes of OPD in the detector plane with OPD in normal

direction. Experimental data from IntelliWave software of Intellium Fizeau interferometer show half of the double pass OPD, and, in case of null testing, it is the topography of the tested surface. In non-null configuration, with increasing deviations from normal incidence, paths of the reflected rays are differing more from the incident ones. Dividing the total OPD into half does not give correct image of what we want to measure: normal direction OPD between the aspherical surface and the reference sphere. Therefore, retrace error can be quantified as a difference between experimental data and theoretical prediction of OPD computed in normal direction. Theoretical calculations were done in Octave program Aspherix.

The spherical surface with radius of curvature $r=19.768$ mm was defocused ± 0.05 mm from the null position. Theoretical Zernike coefficients are the wavefront aberrations in normal direction between sphere defocused copy. Aspherix program also calculates how much of the spherical diameter is actually imaged on the detector; a transmission sphere $F\#=3.3$ is not enough to illuminate the entire diameter.

Another experiment was carried out to check if Intellium built-in optical zoom has an influence on measurements. Ge lens measured in Table 4.6 was used as a test subject. The reflected beam diameter in the best fit position is smaller than aperture of the transmission sphere, thus it was possible to zoom in and zoom out. Reconstructed OPD maps for all cases are compared.

Results

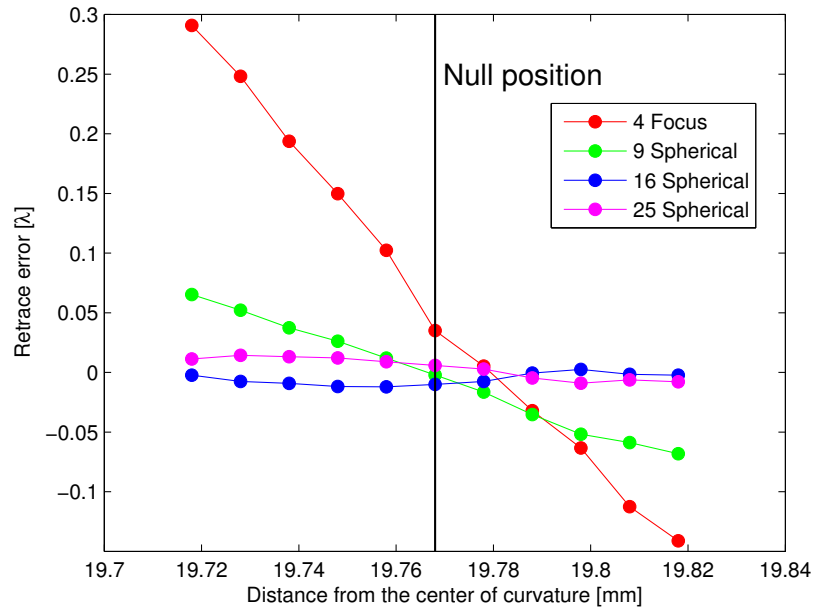


Figure 5.2: Retrace error for defocused sphere with $r=19.768$ mm

The graph in Figure 5.2 indicates that retrace error has an influence on focus and primary spherical aberration, the other rotationally symmetrical Zernike coefficients change is almost zero, it lies below 0.05λ . Focus aberration is the Zernike term mostly influenced by retrace error. Growth of the primary spherical aberration is symmetrical on both sides.

As can be seen from Figure 5.2, the experiment with defocused sphere suggests that retrace error causes a rather slow increase in primary spherical aberration (less than 0.1λ for 0.05 mm of defocus). LENS 7 with very low aspherical coefficients can be approximated by sphere, so we can estimate the retrace error using the graph for defocused sphere. In this case, it is almost null measurement and retrace error is negligible. Ge lens has around three times higher deviation from sphericity than LENS 7 and, in this case, retrace error changes the detected wavefront.

Figure 5.3 confirms that, for asphere, using the optical zoom in non-null measurements can significantly change the shape of detected wavefront, thus also the retrace error. Zooming means changing position of one of interferometric imaging lenses, so the wavefront is modified. Zooming in decreases the detected spherical aberration, zooming out increases.

5.2 Theoretical Approach

Prescription of all components of Twyman-Green interferometer is available in optical design software Zemax. We can check suitability of this tool for measurements of aspheres and how the retrace error affects the detected OPD. The general task stays the same as it was with Fizeau interferometer - to find the best measurement configuration. The solution is found using Zemax optimization tool. This time, the only variable in the system is position of the asphere, the transmission sphere is fixed ($F\#=1.2$). More transmission spheres are yet to be designed. Our request is to measure retrace error, so detected OPD is compared to OPD in normal direction computed in Aspherix program.

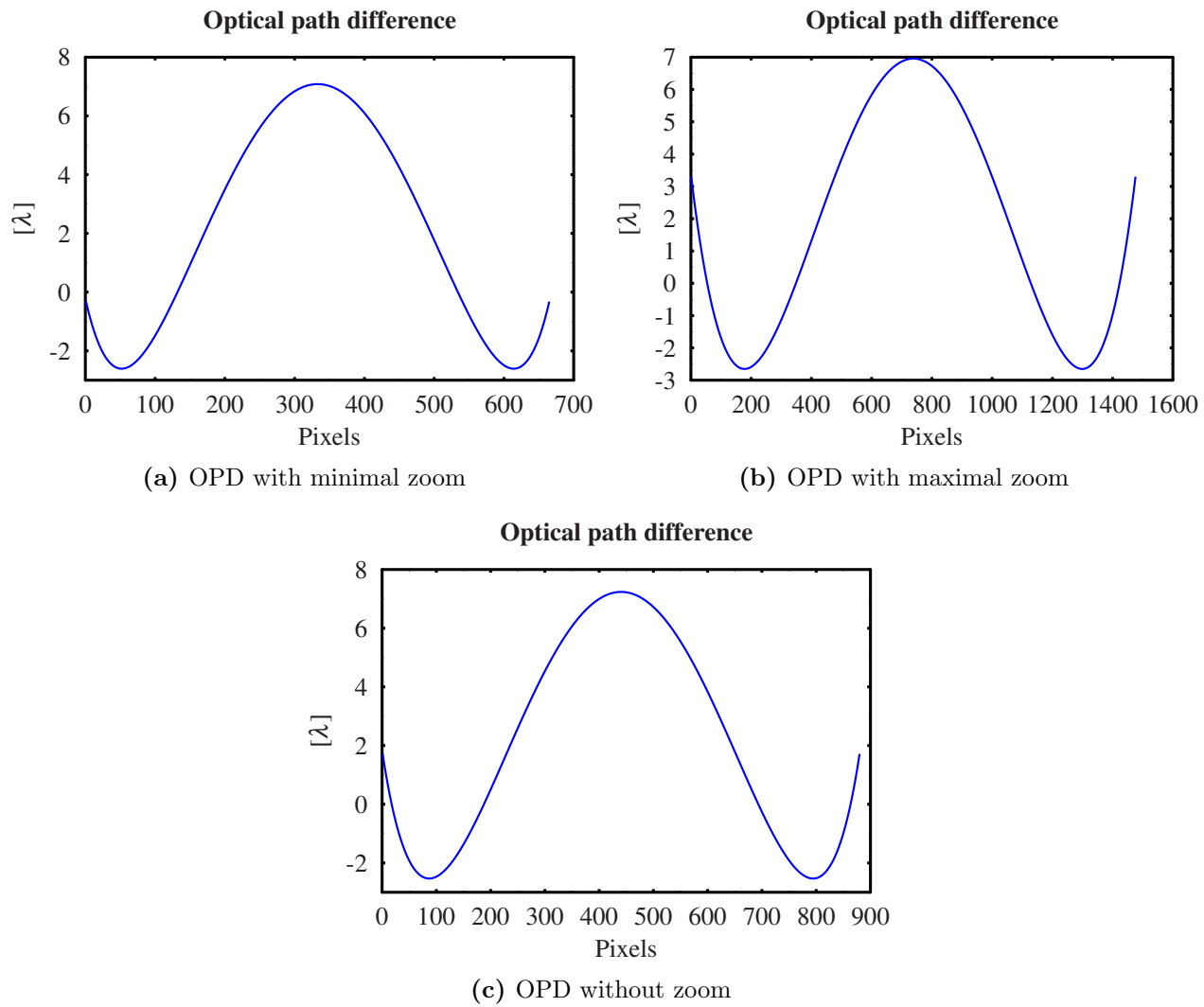


Figure 5.3: Ge lens measurement: results with zoom

	minimal zoom	without zoom	maximal zoom
pixels	665	880	1476
4 Focus	-4.0726	-3.2057	-2.0217
9 Spherical	3.2584	4.2365	5.0543

Table 5.4: Ge lens measurement: results with zoom

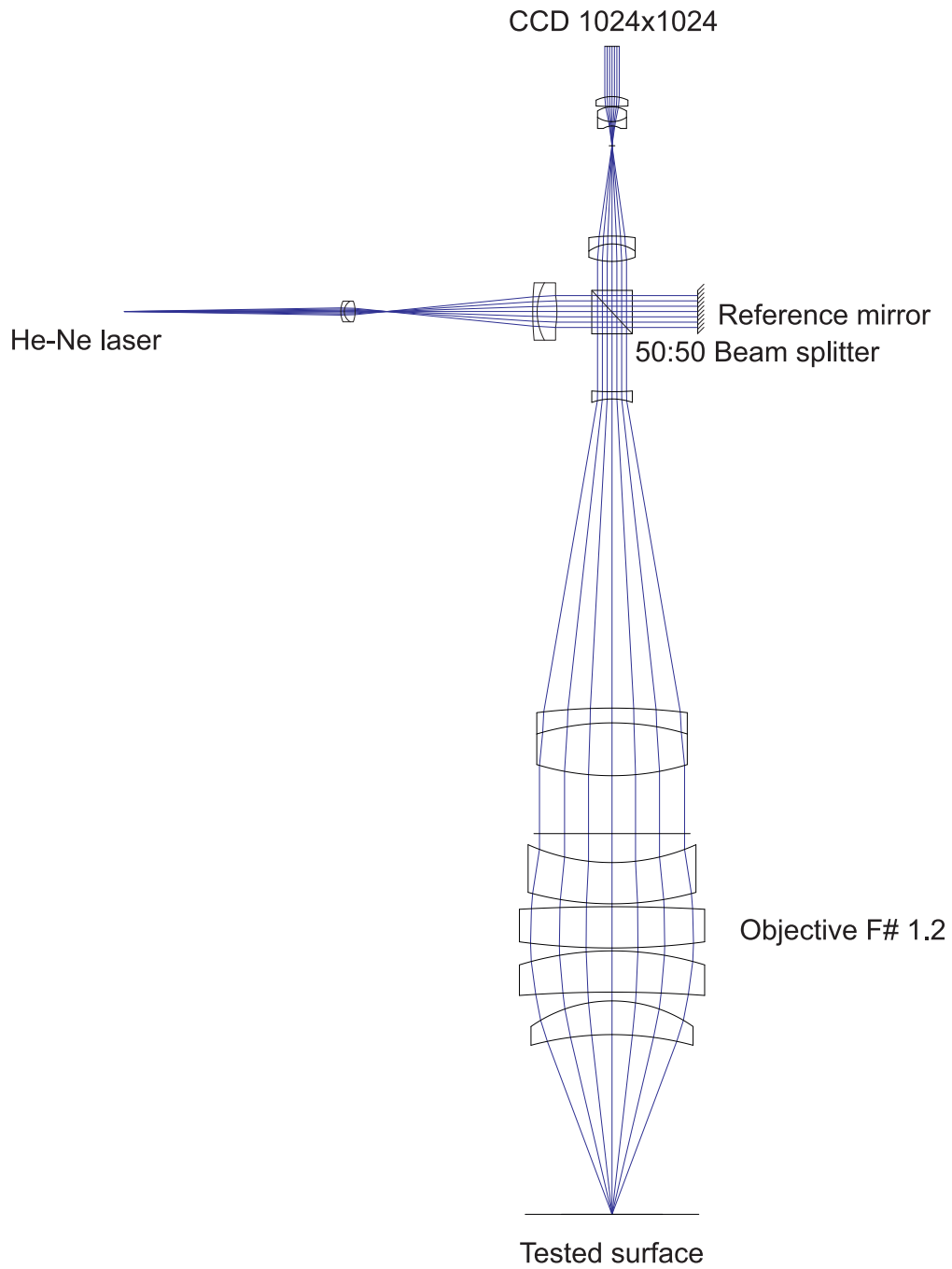


Figure 5.5: Twyman-Green interferometer with the tested surface in cat's eye position

Results

Asphere A3			Zemax	Aspherix	Retrace error
Measured \varnothing 20.1437 mm	Complete \varnothing 23 mm	4 Focus	-45.1593	-39.5602	-5.5991
Zemax best fit 33.023 mm	Aspherix best fit 32.461 mm	9 Spherical	6.5656	16.1259	-9.5603
Zemax OPD PV=79.052 λ	Aspherix OPD PV=79.079 λ	16 Spherical	8.2311	1.00138	7.2297
		25 Spherical	2.7867	0.1443	2.6424
		36 Spherical	0.5919	-0.0026	0.5945

Table 5.1: Retrace error for asphere A3 measured on Twyman-Green interferometer

Asphere A4			Zemax	Aspherix	Retrace error
Measured \varnothing 10.494 mm	Complete \varnothing 22 mm	4 Focus	-0.2335	-0.8989	0.6654
Zemax best fit 15.521 mm	Aspherix best fit 15.62 mm	9 Spherical	2.4825	1.7806	0.7018
Zemax OPD PV=3.95 λ	Aspherix OPD PV=3.6448 λ	16 Spherical	0.3699	0.0028	0.3671
		25 Spherical	0.0526	0.002	0.0506
		36 Spherical	0.008367	-0.00003	0.0084

Table 5.2: Retrace error for asphere A4 measured on Twyman-Green interferometer

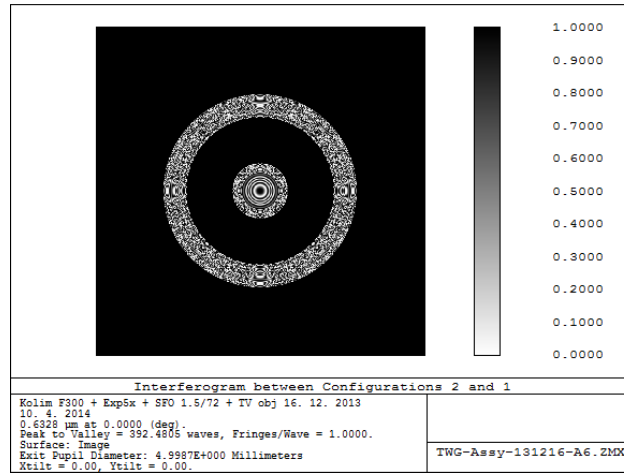


Figure 5.6: Interferogram for asphere A6; rays reflected from the middle part are cut off by system apertures

Overall, Zemax simulations showed that this interferometer with $F\#=1.2$ is not a good instrument for testing of aspheres. Aperture of the transmission sphere is insufficient to illuminate entire diameter of tested surface. Due to short focal distance, aspheres with large vertex radius of curvature cannot be placed in the best fit position (eg. LENS 7, Ge lens). With $F\#=1.2$, the part of reflected aspherical wavefront does not even reach the detector in most of the cases (the typical interferogram looks like Figure 5.6). However, the biggest problem is insufficient chip resolution. Asphere A3 example is shown as a typical case. Even when the position where most of reflected rays reach the detector is found, wavefront slope still violates the Nyquist condition. Aspherical departure from the planar wavefront reaches usually around 70λ . As Table 5.2 shows, aspherical wavefront changed its shape after passing interferometer optics; higher order aberrations become more important. Retrace errors are obviously large as well when the shape of the wavefront becomes completely different. The only asphere which can be measured using Twyman-Green is A4, but only around half of its diameter. This asphericity will still cause retrace errors 0.7λ for primary spherical aberration. At Twyman-Green interferometer, retrace error is not negligible even when a wavefront with low asphericity is imaged.

Possible upgrade to make this setup more suitable for measurement of aspheres is using a different transmission sphere with higher $F\#$ or detector with higher resolution.

5.3 Discussion

To sum up, all previous results confirm non-null testing method can give satisfying results only in case of weak aspheres. The only lens successfully measured on Intellium Fizeau interferometer is LENS 7, which has the lowest coefficients of asphericity from all the aspheres in MEOPTA. For the rest, disadvantages of non-null testing become significant. The deviation of reflected rays from the incident ones might cause they do not reach the detector at all. In the opposite case, they take a different path in the imaging optics and add up system aberrations to the wavefront. Indeed, retrace error has an impact on results in non-null measurement of aspheres and it definitely needs to be considered in data analysis. In the measurement of aspherical surface of LENS 7, it can be neglected due to fortunate combination of conditions: big vertex radius of curvature and low asphericity. All together, we came to the conclusion that full prescription of the optics inside measuring instrument is absolutely necessary for testing of aspheres. As predicted, moving one lens in the interferometer (zooming) proves that retrace error affects the results.

It is clear that interferometer must be calibrated for useful measurements of aspheres. The Aspherix program can be a starting point for writing macro in Zemax programming language which can calculate the optimal measurement conditions. With the full knowledge of system parameters, the detected wavefront shape can be predicted and separated from measurements. Influence of retrace error will be included in final OPD after an entire system is raytraced.

More simulations need to be done to find out how much tilt and decenter of optical elements in-

fluence the final OPD. More accurate calibration method which we suggest to use in the future is reverse optimization. The conventional task for lens design program is to find the system parameters which meet the designer's requirements for the system performance. In reverse optimization, the real system performance is measured first. Zernike coefficients of OPD are set as optimization operands together with tilts and decenters of elements, position of test surface. Afterwards, the optimization process adjusts the variables in order to reach the minimal deviation between actual and measured OPD. Parameters of the interferometer optics must be known better than their design prescriptions and tolerances allow to achieve more accurate results.

Since interferometric testing with non-adapted wavefront was not proven as reliable and universal method, we decided to invest the time into designing a null compensator. If it is possible to design it in a simple way and the compensation is efficient, the advantages of having accurate method to test important aspheres outweigh the cost and designing difficulties.

Chapter 6

Null Testing

As discussed in the previous chapter, retrace error has a significant influence on the results in non-null aspherical testing. Since we are not able to exactly quantify its influence in testing of aspheres on Intellium interferometer, the concept of null testing which seemed nontrivial is now reconsidered as next method to try. The designed null component should minimize differences between reference and reflected wavefront. The compensator modifies the paths of rays and shapes the transmitted wavefront. This results in the incident rays reaching the aspherical surface in the normal direction, following the same path on the way back. For this reason retrace error approaches zero and does not have to be considered in further analysis. In the ideal case, all system optics aberration cancel out and have no effect on the measurement.

Simple null compensators consisting of only one lens were designed for aspheres available in MEOPTA. The results are presented in this chapter.

6.1 Optical Design and Tolerancing

Up to the late 1940s, all optical designs had to be made by hand calculation. This method was very tedious and time-consuming. Probably the earliest use of a computer to trace rays was by James G. Baker in 1944, who used the Mark I calculator at Harvard to trace rays. Later on, with the start of computer era, faster computations opened the new possibilities in the lens design. Even after the years of development, present lens design programs are still far from being completely automatic. The experience and proper knowledge are essential to operate them correctly.

Optical components are designed using the program's optimization tool. The optimization function takes a starting design and modifies its construction so that it meets a given set of specifications. The starting design may be the result of a previous design task, combination of catalog lenses or a brand new design based on the designer's experience and intuition. The performance of the design is evaluated by outcome of single error function called **merit function**. The merit function is the sum of squares of desired system attributes called operands. It can be defined in many manners, e.g. geometrical spot size, root mean square deviation of detected wavefront or desired behavior of modulation transfer function. The operands put the constraints on the system performance.

Typical operands are, for instance, the maximal value of spherical aberration, ray heights of certain rays, exact value of focal distance.

The program iteratively adjusts the system constructional parameters - radii of curvature, glass thickness, diameters, coefficients of asphericity, refractive index, etc. The optimization process uses them as variables and finds the solution which collectively minimizes the deviations of actual operand values from the target. It is not very probable that solution makes all of the operands equal to their target values. The importance of each operand forming the merit function is controlled by weight factors. Not all of the operands need to be exactly satisfied. If the factor is larger, the variables affecting the operand do not change a lot. Obviously, the variables affecting the operand with smaller weights can get values far from the initial guess.

Usually the operands depend on the given variables nonlinearly. From the mathematical point of view, this property leads to difficult nonlinear least-squares optimization. The final solution of nonlinear equations depends on the initial conditions, so well chosen input values can considerably reduce the computation time. Unfortunately, the program cannot find the global minimum, it finds the local minimum influenced by initial conditions. Sometimes the system reaches the stagnation point where the program cannot find any solution independently of number of iterations. The merit function value does not seem to change and minimization is too low to be helpful. To overcome this issue, the different initial conditions have to be entered to the program.

The optical design does not finish with the successful optimization. In reality, the optical and mechanical components can never be made perfectly, so determination of the tolerance upon the system is even more important task. The system must keep a good performance when the variables have the values in the reasonable range. The tolerances for dimensions and product properties are a part of the standardized way of communication between the optical designer and the technologist. Without a standard method for describing the details of the part, there is no guarantee that the designer will end up with a part which matches his/her specifications [43].

The most commonly used standard in the industry is ISO 10110. It describes the preparation of drawings for optical elements and systems. Each part covers a different aspect of the optical drawing. Typical manufacturing tolerances in a lens system are listed in Table 6.1.

Parameter	Commercial	Precision	High precision
Wavefront residual RMS	0.25 λ	0.1 λ	<0.07 λ
Thickness	0.1 mm	0.01 mm	0.001 mm
Radius	1 %	0.1 %	0.01 %
Index of refraction	0.001	0.0001	0.00001
Abbe number	1 %	0.1 %	0.01 %
Decenter	0.1 mm	0.01 mm	0.001
Tilt	1'	10"	1"
Sphericity	2 rings	1 ring	0.25 ring
Irregularity	1 ring	0.25 ring	<0.1 ring

Table 6.1: Typical values of tolerances in a lens system [3]

6.2 Null Compensators for Aspheres

The very best option for null testing is having a reference surface for comparison. The quality of the reference needs to be better than quality of any tested surface. Unfortunately, aspherics with sufficient quality cannot be manufactured in MEOPTA yet. The degree of compensation of wave-front aberrations depends on the quality of all surfaces involved. Deformations of spherical/planar surfaces can be easily checked using interferometers, so it is preferable to design a compensating element without special surfaces. MEOPTA usually reaches $\lambda/20$ precision for spheres and $\lambda/30$ for planes, which is sufficient for null measurements.

Another aspect to consider was whether the compensator should be reflective or refractive. It would be difficult to set correct off-axis alignment with the equipment available in the laboratory, so there are two possibilities of our next approach. The first one is to put the aspherical lens in between the transmission sphere and compensating mirror. The other one requires refractive compensating element and aspherical surface is measured in reflection. The second option was chosen because it is easier for the optimization. In the first one, there are only four parameters to vary - the position of the aspherical lens (distance to transmission sphere and to the reflective compensator), orientation of aspherical lens (which surface refracts first) and the radius of curvature of the mirror. While designing the refractive null compensator as single refractive element, apart from its position in the setup we can alter both radii, the lens thickness and the glass type. With more parameters to change, there is a higher chance that a combination, which meet our demands, exists.

Generally, our goal is to design sufficient null compensator as simple as possible. The compensating element was designed using optical illumination software Zemax using its extensive built-in optimization and tolerancing tools. We assume that the greater part of the aberration introduced by the asphere is of low order. This condition makes it easier to get good compensation with a single element of convenient form. For this reason our compensator consists of only one lens with planar/spherical surfaces manufactured from the common type of optical glass BK7.

Spherical reference optics used with Fizeau interferometer was replaced by perfect lens in the simulations because the exact transmission sphere design is not available. The double-pass system was optimized for compensator radii, thickness and compensator position between the asphere and transmission sphere. All three transmission spheres were considered. It is required that the compensation must work well for entire diameter of aspherical surface. This condition seems very strict for aspheres strongly differing from spheres or with large diameter.

6.3 Optimization Results

Optimization was successful for three out of ten aspheres available. LENS 7 was not included since it was proven no compensating elements are necessary to measure the topography of the aspherical surface. As predicted, it was not possible to compensate strongly aspherical wavefronts. All three lenses have one common feature - big radius of curvature (A1:ra=-185.5253 mm, A8: ra=164.3958 mm, A11: ra=184.882 mm). They make the least aspherical wavefront after the reflection. It seems like the coefficients of asphericity do not have as big influence in the optimization process as the radius of curvature. Actually, the asphere A1 has one of the highest coefficients $A_2 = 8.9 \cdot 10^{-5}$. A1 compensating element works as a diverging lens, the rest is converging (A1 is a concave surface and it focuses the reflection). We found out that the objectives available for measurements are not sufficient to approach the normal incidence of incident rays. Using the transmission sphere with higher F# would lower the angle of incidence (without using additional lens).

The compensator shapes and positions are shown below. The wavefront errors after the compensations are less than 0.035λ , the residual spherical aberration is less than 0.02λ .

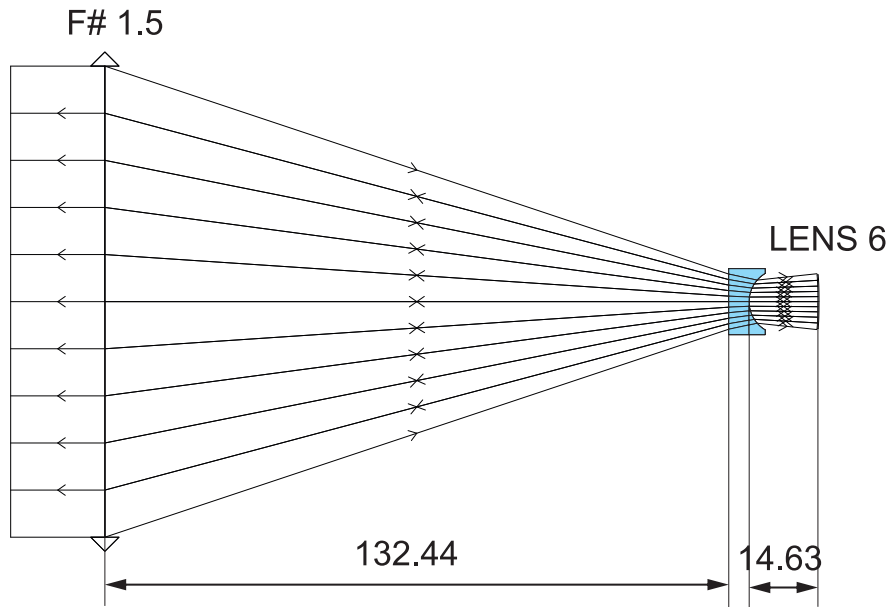


Figure 6.1: A1 null compensator placed in the correct position

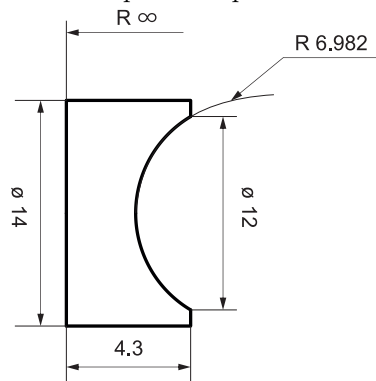


Figure 6.2: A1 null compensator

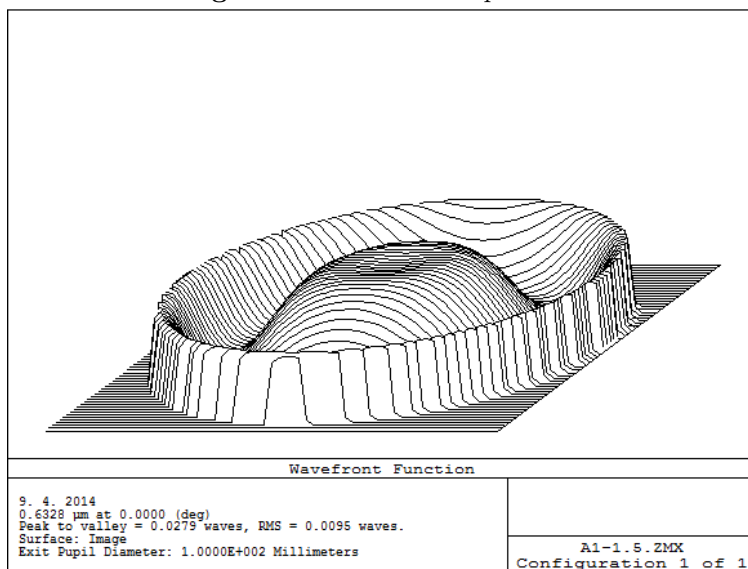


Figure 6.3: Residuals after compensation of asphericity

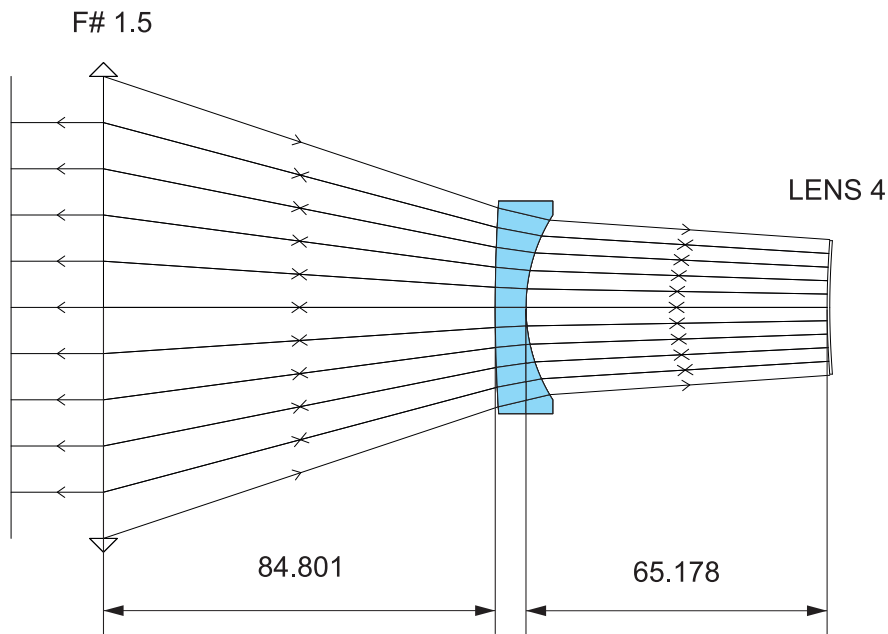


Figure 6.4: A8 null compensator placed in the correct position

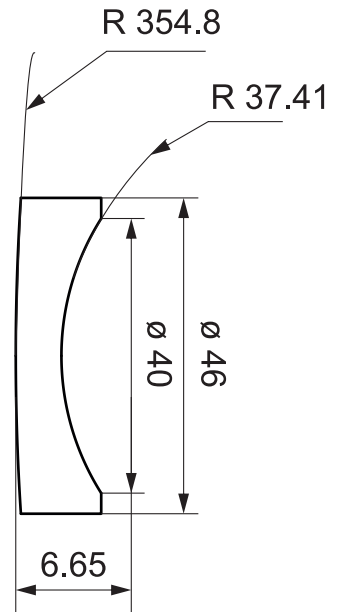


Figure 6.5: A8 null compensator

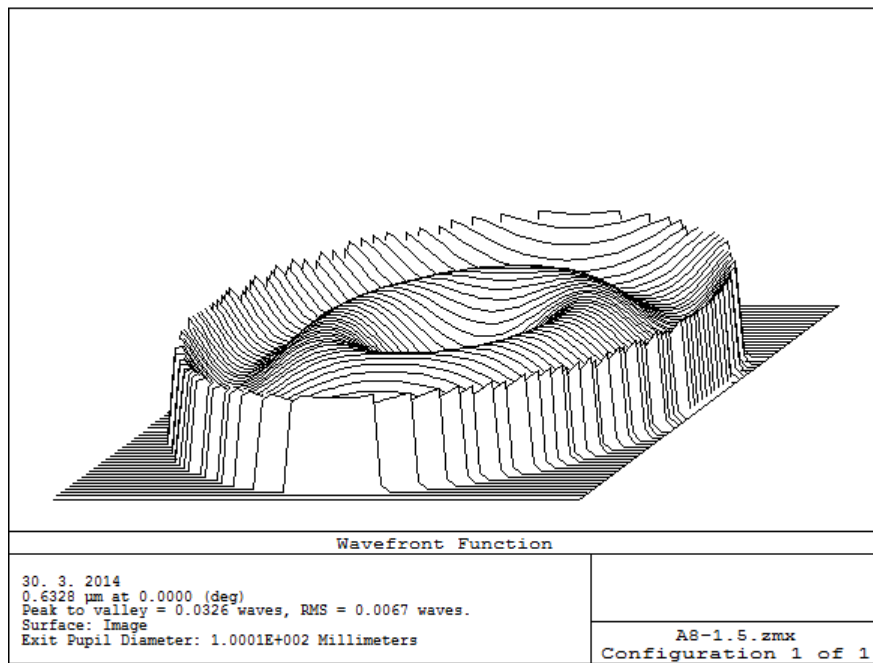


Figure 6.6: Residuals after compensation of asphericity

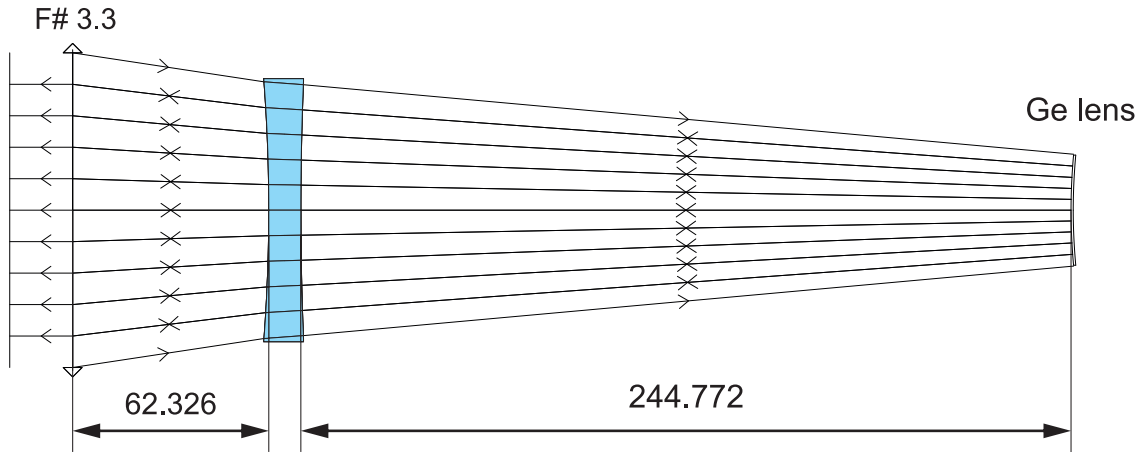


Figure 6.7: A11 null compensator placed in the correct position

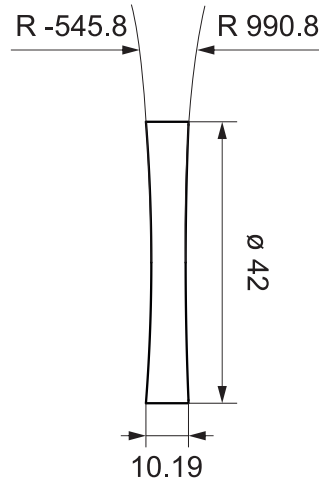


Figure 6.8: A11 null compensator

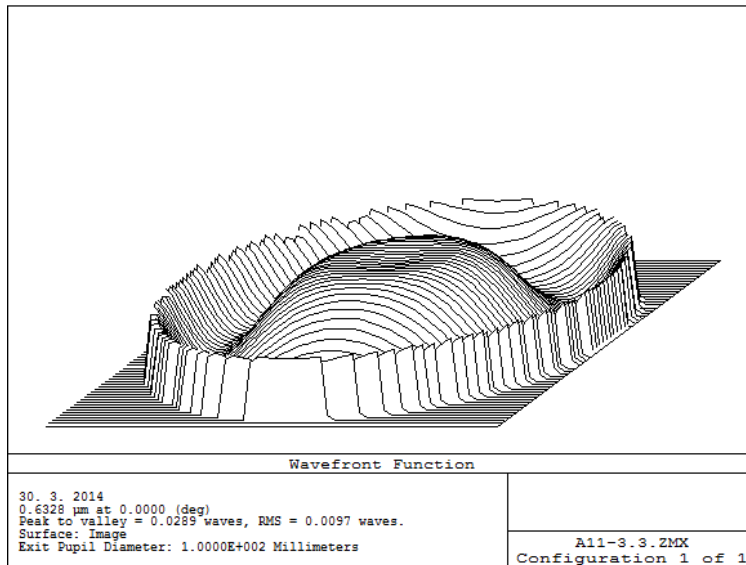


Figure 6.9: Residuals after compensation of asphericity

Asphere A1 (in the drawing named as LENS 6) has the highest asphericity out of three aspheres for which the compensating element was designed. For this reason, the compensator for LENS 6 was the one chosen to be manufactured.

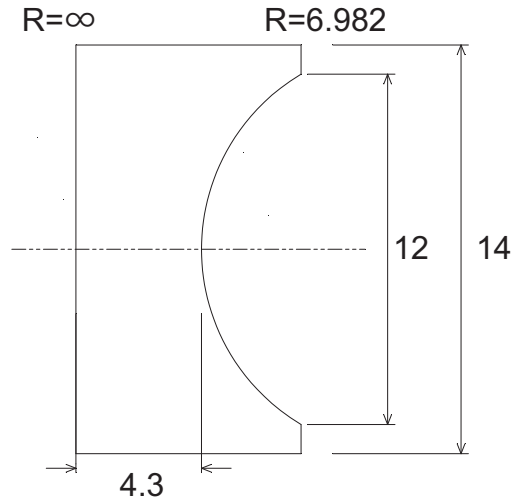


Figure 6.10: Null compensator for LENS 6

6.3.1 Reflectivity of Aspherical Surface

In suggested null configuration, the aspherical surface is a reflective component, so it is necessary to characterize its reflectivity. Fizeau interferometers generate an interference between the surface of a test sample and a reference surface. The interference image is recorded and analysed by an imaging optics system. The contrast of the interference signals depend, however, on the reflectivity of the test samples. Both beams should have similar intensities to get high contrast of fringes. The reference beam is reflected from the last surface of the transmission sphere. There is no antireflection coating; the standard glass-air interface reflectivity is around 4 %. According to optical drawing, both surfaces of aspherical lens are antireflection coated for the wavelengths ranging from 650 nm to 950 nm. A manufacturer claims that maximum reflectivity in this range is 0.5 % for the aspherical surface and 1 % for the spherical surface. Luckily, the antireflection coating was optimized for central wavelength around 800 nm and quite broad bandwidth, which most likely indicates the quick increase of reflectivity outside the bandwidth. The reflectivity of LENS 6 aspherical surface for the wavelength we use for testing (632.8 nm) is not known, but as measurement showed, it is sufficient to give a good contrast of interference fringes.

6.3.2 Tolerance Analysis

The result of optimization with very precisely calculated values of radii, glass thickness and distances needs to be adjusted; in reality, such high precision is not possible to reach.

The radii of curvature were not chosen arbitrarily. There is a finite number of optical calibers according to ČSN 19 0425 standard, so choosing the radius from the catalog would speed up the

manufacturing process. One of the radii is replaced by the most similar radius from the catalog and the system is re-optimized with the same conditions. Then, the other radius is fixed to the catalog value and again, the optimization with the remaining variables is done. This manual iterative process finishes when the best combination of catalog radii is found.

Tolerance analysis is important to set limits for the manufacturing process. As a first step, constraints on the radii of curvature, glass and air thicknesses, refractive index and Abbe number of the glass were set. Any change in one of the parameters can be later still optimized by readjusting the position of entire mechanical device.

Tolerance for tilts and decenters in the system was examined separately. The system was tolerated for centricity of compensating lens (TUTX 4, TUTY 4), centricity of the asphere (TUTX 9, TUTY 9, 1' from the drawing), decenter and tilt between optical axes of both lenses (TUDX 2, TUDY 2). Compensation is considered as sufficient if the RMS value of the residuals does not exceed 0.1λ .

TFRN 3	Tolerance on second radius of curvature of compensating lens	± 4 fringes
TFRN 4	Tolerance on aspherical radius of curvature (from the drawing)	± 4 fringes
TTHI 2	Glass thickness	± 0.05 mm
TTHI 3	Air thickness between compensator and asphere	± 0.1 mm
TIND 2	Refractive index of glass	± 0.0005
TABB 2	Abbe number of glass	± 1 %

Table 6.2: Tolerances for the compensating element of LENS 6

Tolerance analysis shows that the most critical parameters are the distance between compensator and asphere. RMS is also very sensitive to any decenter between lenses. A solution how to fix the position and make the optical axes aligned is placing the lenses in mechanics.

Analysis of Tolerances

Criterion : RMS Wavefront Error in waves
 Nominal Criterion : 0.00496883
 Test Wavelength : 0.6328

Worst offenders:

Type			Value	Criterion	Change
TTHI	3	1	-0.10000000	4.66115086	4.65618203
TTHI	3	1	0.10000000	4.56037073	4.55540190
TFRN	4		-4.00000000	1.35100480	1.34603597
TFRN	4		4.00000000	1.31061294	1.30564411
TIND	2		-0.00050000	0.91593884	0.91097001
TIND	2		0.00050000	0.89803453	0.89306571
TTHI	2	1	-0.05000000	0.89479926	0.88983043
TTHI	2	1	0.05000000	0.87996965	0.87500082
TFRN	3		-4.00000000	0.61844430	0.61347547
TFRN	3		4.00000000	0.60327253	0.59830370

Monte Carlo Analysis:

Trial	Criterion	Change	Optimized
1	1.30216886	1.29720003	0.028
2	0.88906268	0.88409385	0.0348
3	3.42563422	3.42066540	0.126
4	0.61103685	0.60606802	0.0762
5	0.19875382	0.19378499	0.10004
6	1.96898499	1.96401616	0.0102
7	0.11038697	0.10541814	0.0078
8	1.89896362	1.89399479	0.0417
9	2.12090128	2.11593245	0.0077
10	3.29636401	3.29139518	0.041
11	1.09133173	1.08636290	0.0148
12	0.25056829	0.24559946	0.0251
13	3.29598691	3.29101808	0.0889
14	1.71214128	1.70717245	0.0577
15	2.26746571	2.26249688	0.0108
16	0.82883917	0.82387034	0.0106
17	2.32731092	2.32234209	0.0599
18	0.49317647	0.48820764	0.0568
19	1.09628864	1.09131981	0.0215
20	4.28540222	4.28043339	0.0029

Table 6.3: Tolerance analysis results (without tilts and decenters)

Analysis of Tolerances

Criterion : RMS Wavefront Error in waves
 Nominal Criterion : 0.00496883
 Test Wavelength : 0.6328

Worst offenders:

Type		Value	Criterion	Change
TUDX	2	0.01000000	0.31519090	0.30529674
TUDX	2	-0.01000000	0.31519090	0.30529674
TUDY	2	0.01000000	0.31519089	0.30529673
TUDY	2	-0.01000000	0.31519089	0.30529673
TUTY	9	0.02000000	0.12176943	0.11187527
TUTY	9	-0.02000000	0.12176943	0.11187527
TUTX	9	0.02000000	0.12176943	0.11187527
TUTX	9	-0.02000000	0.12176943	0.11187527
TUTX	4	0.02000000	0.07743054	0.06753639
TUTX	4	-0.02000000	0.07743054	0.06753639

Monte Carlo Analysis:

Trial	Criterion	Change
1	0.20552623	0.19563207
2	0.26597284	0.25607869
3	0.07324431	0.06335015
4	0.20449178	0.19459763
5	0.12546117	0.11556702
6	0.22529735	0.21540319
7	0.18483055	0.17493639
8	0.21393267	0.20403851
9	0.22702532	0.21713116
10	0.14652946	0.13663530
11	0.04407165	0.03417750
12	0.27640221	0.26650805
13	0.35975181	0.34985766
14	0.39198553	0.38209137
15	0.39893056	0.38903641
16	0.20577322	0.19587906
17	0.09236110	0.08246694
18	0.04795040	0.03805625
19	0.09988498	0.08999082
20	0.28468267	0.27478852

Table 6.4: Tolerance analysis results (tilts and decenters)

6.3.3 Mechanics for Null Component

In practice, the desired distance between the components in the null measurement is difficult to reach. Eliminating tilt and decenter in the system is even more complex task to solve. As a result, the mechanical device was designed in MEOPTA to remove some degrees of freedom for the final null testing. Both lenses (compensating lens and asphere) are inserted into a custom-made tube (Figure 6.11). Its design and dimensions were chosen to keep the distance between the lenses fixed for 14.63 mm. Zemax tolerance analysis in Table 6.3 also confirms that this distance is the worst offender in tolerancing process, that is why the mechanical tolerance for set for ± 0.01 mm.

At first, the compensating lens is centered to the outside diameter of the tube. The non-centricity of the lens itself must be as low as possible, the mechanics cannot compensate for it. Next, the lens is cemented in the best centered position, which is why the tube has three side holes.

The aspherical lens is removable for the purpose of optical testing. Nevertheless, it needs to be fixed in the tube and properly aligned with the compensating lens. Its position in the mechanics is set by two rings placed on the edge of the spherical surface. One of them is held by the external thread in the tube. We assume that asphere itself has zero centricity error.

The tube is made of free-cutting steel with material number 1.0715, all the surfaces are blacked to suppress any stray light reflections. The material is described as free-cutting steel for bulk applications for joining elements in mechanical engineering and automotive components [44]. The ring touching the spherical surface is made of flexon to prevent the damage, the threaded one is made of alloy.

The only degrees of freedom left now are the tilt, decenter and position of the entire device. Unfortunately, tolerance analysis shows that even very strict constraints for surface tilts ($1'$) and decenters (0.01 mm) cross the limit of resulting $\text{RMS}=0.1 \lambda$. The tilts and decenters of lenses with respect to the axis of mechanical device need to be measured and later subtracted from the measurement.

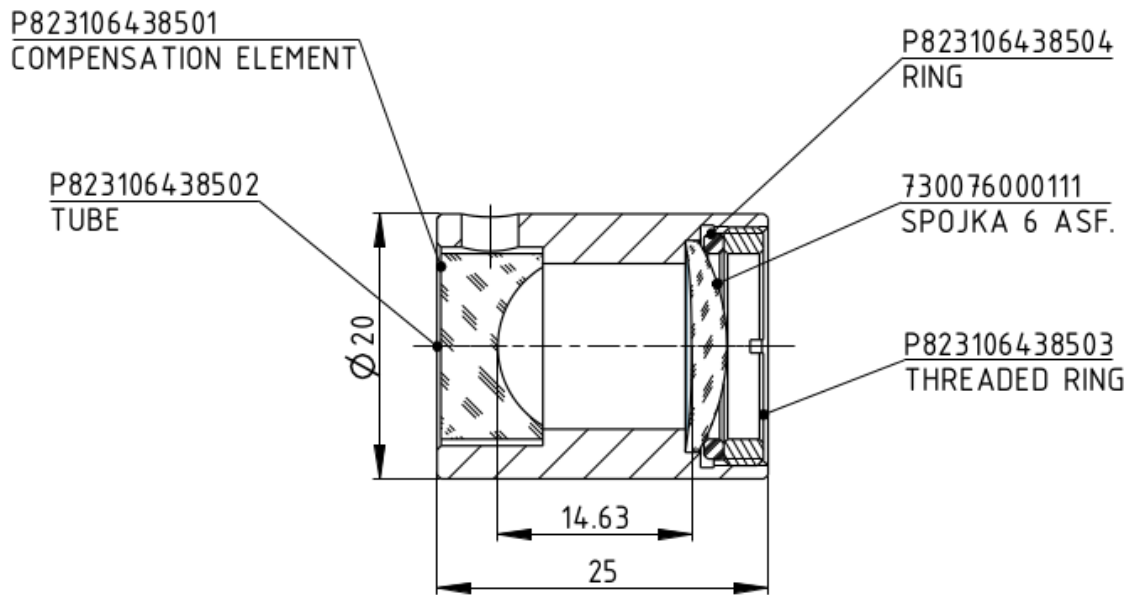


Figure 6.11: Mechanical device for null measurement, complete drawing is in Appendix D

Simple refractive null compensators for three aspheres were designed in Zemax. When they are placed in between the transmission sphere of Intellium interferometer and tested asphere and properly aligned, they should compensate the asphericity of detected wavefront. The PV of the wavefront after compensation does not exceed to 0.04λ . Compensator for LENS 6, in form of plan-concave lens, is about to be manufactured and tested in the future. Mechanical device for testing with this compensator was designed as well.

Chapter 7

Conclusion

This thesis reviewed the efficiency of technologies available in Optical metrology department in MEOPTA for aspherical testing. The task required coding an own program in Octave for theoretical simulations, which were compared to experimental results.

Two devices were used for aspherical testing: Intellium Fizeau interferometer and HASO Shack-Hartmann sensor. Their limitations were found by simulating the measurement in the Octave program. A short list of aspherical lenses included in MEOPTA products was tested on both devices and the performance of two different wavefront detection methods was analyzed. Phase shifting interferometry was suggested to be used in the future experiments due to its higher dynamic range and better spatial resolution.

Method for testing aspheres with spherical reference on Intellium interferometer was proposed in this thesis. Analysis of surface deformations relies on the outcome of ray tracing simulation in Octave program. The program provides the wavefront to be subtracted from the wavefront reconstructed by IntelliWave software using phase shifting method. Theoretical predictions suggested two aspheres from the list that could be measured in non-null setup.

The results were positive in case of asphere LENS 7, which has the lowest coefficient of asphericity from all available aspheres. Surface deformations of the other lens, made from Germanium, were not evaluated correctly. Even though a wavefront reflected from the test surface was successfully reconstructed, a mismatch between observed shape and its theoretical prediction appeared. This raised a question about the accuracy of simulation. The possible missing factor which was not considered is the influence of retrace error - aberrations introduced by interferometer optics in non-null testing setup.

Since it was not possible to work with prescription of Intellium interferometer optics, retrace error was not precisely quantified. Simulations on Twyman-Green interferometer, soon to be assembled in MEOPTA, showed that retrace error cannot be neglected and it has a strong impact in non-null testing of aspheres. Using Intellium Fizeau interferometer with spherical reference beam is a good option for aspherical testing only for very weak aspheres (with coefficient $A_2 \sim 10^{-7}$). In general, analysis of data from non-null testing requires the full information about the system which must be

completely raytraced.

Testing aspheres with spherical wavefront was proven to be inefficient. Nevertheless, Intellium interferometer can still be used in the future with special beam shaping optics. Three simple refractive null compensators were designed minimizing the asphericity of detected wavefront. Compensating element for LENS 6 asphere in the shape of plan-concave lens is currently being manufactured and will be tested afterwards. If the quality of surfaces is sufficient, it will be placed in a mechanical device together with the asphere to fix their relative position. Then, if aspherical testing with null compensator will give satisfying results, the benefits will outweigh the costs of manufacturing the lens.

Appendix A

List of Aspheres Used in MEOPTA

$z_a = \frac{\frac{1}{r_a} \cdot S^2}{1 + \sqrt{1 - (K + 1) \left(\frac{1}{r_a}\right)^2 S^2}} + \sum_{i=1}^4 A_i S^{2i}$	A1 SPOJKA 6 ASF. 730 0760 00111	A2 LENS 1 07300760009110	A3 LENS 6 07300760010110
Optical diameter d	11.4	22.8	23
Radius of curvature ra	-185.5253	32.71039	30.89927
Conic constant K	0	-1.39446	0.36221
Coefficient of asphericity A_1	0	0	0
Coefficient of asphericity A_2	8.95734e-5	-1.165537e-5	-6.760244e-6
Coefficient of asphericity A_3	0	-3.726022e-8	-3.420194e-9
Coefficient of asphericity A_4	0	-7.747244e-11	-7.387291e-11

$z_a = \frac{\frac{1}{r_a} \cdot S^2}{1 + \sqrt{1 - (K + 1) \left(\frac{1}{r_a}\right)^2 S^2}} + \sum_{i=1}^4 A_i S^{2i}$	A4 LENS 1 - ASP 07300760006110	A5 LENS 4 - ASP 07300760007110	A6 LENS 6 - ASP 07300760008110
Optical diameter d	22	13.6	16.6
Radius of curvature ra	15.3817	43.947	-58.4325
Conic constant K	-0.13889	-0.03818	0
Coefficient of asphericity A_1	0	0	0
Coefficient of asphericity A_2	-4.841939e-6	-4.076374e-5	-2.02409e-4
Coefficient of asphericity A_3	5.833533e-9	-2.685245e-7	-2.625569e-7
Coefficient of asphericity A_4	-1.673422e-10	-2.562076e-9	1.039743e-8

$z_a = \frac{\frac{1}{r_a} \cdot S^2}{1 + \sqrt{1 - (K + 1) \left(\frac{1}{r_a}\right)^2 S^2}} + \sum_{i=1}^4 A_i S^{2i}$	A7 LENS 8 ASPH 730 0760 00488	A8 LENS 4 730 0760 00288	A9 LENS 7 730 0760 00388
Optical diameter d	11.4	28.9	35
Radius of curvature ra	-24.43	164.3958	133.2126
Conic constant K	-10	0	0
Coefficient of asphericity A_1	0	0	0
Coefficient of asphericity A_2	-3.0574139e-5	-1.16455137e-6	-2.6934596e-7
Coefficient of asphericity A_3	7.3835473e-7	1.1766029e-10	4.0803344e-10
Coefficient of asphericity A_4	0	0	0

$z_a = \frac{\frac{1}{r_a} \cdot S^2}{1 + \sqrt{1 - (K + 1) \left(\frac{1}{r_a}\right)^2 S^2}} + \sum_{i=1}^4 A_i S^{2i}$	A10 ROZPTYLKA 5 760342	A11 Ge lens
Optical diameter d	23	35
Radius of curvature ra	-21.22	184.882
Conic constant K	0	0
Coefficient of asphericity A_1	0	-4.725e-6
Coefficient of asphericity A_2	4.13e-5	-2.972e-7
Coefficient of asphericity A_3	0	5.26e-11
Coefficient of asphericity A_4	0	0

Appendix B

Zernike Frindge Coefficients

U of A Zernike Polynomial Set

$N(r)$ = polynomial order by r , $M(t)$ = polynomial order by t ,

$L(r,t)$ = polynomial order by (r,t) , K = term number

Numbers in **BOLD** are superscripted. For example: r^2 is $SQR(r)$.

$N(r)$	$M(t)$	$L(r,t)$	K	Polynomial
0	0	1	1	1
1	1	2	2	$r \cos(t)$
1	1		3	$r \sin(t)$
2	0		4	$2r^2 - 1$
2	2	4	5	$r^2 \cos 2t$
2	2		6	$r^2 \sin 2t$
3	1		7	$(3r^2 - 2) r \cos(t)$
3	1		8	$(3r^2 - 2) r \sin(t)$
4	0		9	$6r^4 - 6r^2 + 1$
3	3	6	10	$r^3 \cos 3t$
3	3		11	$r^3 \sin 3t$
4	2		12	$(4r^2 - 3) r^2 \cos 2t$
4	2		13	$(4r^2 - 3) r^2 \sin 2t$
5	1		14	$(10r^4 - 12r^2 + 3) r \cos(t)$
5	1		15	$(10r^4 - 12r^2 + 3) r \sin(t)$
6	0		16	$20r^6 - 30r^4 + 12r^2 - 1$
4	4	8	17	$r^4 \cos 4t$
4	4		18	$r^4 \sin 4t$
5	3		19	$(5r^2 - 4) r^3 \cos 3t$
5	3		20	$(5r^2 - 4) r^3 \sin 3t$
6	2		21	$(15r^4 - 20r^2 + 6) r^2 \cos 2t$
6	2		22	$(15r^4 - 20r^2 + 6) r^2 \sin 2t$
7	1		23	$(35r^6 - 60r^4 + 30r^2 - 4) r \cos(t)$
7	1		24	$(35r^6 - 60r^4 + 30r^2 - 4) r \sin(t)$
8	0		25	$70r^8 - 140r^6 + 90r^4 - 20r^2 + 1$
5	5	10	26	$r^5 \cos 5t$
5	5		27	$r^5 \sin 5t$
6	4		28	$(6r^2 - 5) r^4 \cos 4t$
6	4		29	$(6r^2 - 5) r^4 \sin 4t$
7	3		30	$(21r^4 - 30r^2 + 10) r^3 \cos 3t$
7	3		31	$(21r^4 - 30r^2 + 10) r^3 \sin 3t$
8	2		32	$(56r^6 - 105r^4 + 60r^2 - 10) r^2 \cos 2t$
8	2		33	$(56r^6 - 105r^4 + 60r^2 - 10) r^2 \sin 2t$
9	1		34	$(126r^8 - 280r^6 + 210r^4 - 60r^2 + 5) r \cos(t)$
9	1		35	$(126r^8 - 280r^6 + 210r^4 - 60r^2 + 5) r \sin(t)$
10	0		36	$252r^{10} - 630r^8 + 560r^6 - 210r^4 + 30r^2 - 1$

Figure B.1: Page is from Intelliwave software manual [39]

Appendix C

LENS 7: Measurement Protocol from Asphericon

Z490 GPI Application

Z490 Surface/Wavefront Map

Z490 ISO 10110-5: 3/SAG(IRR/RSI) RMSx

SAG: 1.32 fr RMT: fr
 IRR: 0.79 fr RMSi: 0.11 fr
 RSI: 0.20 fr RMSa: fr

Radius (nominal): 0 mm
 Radius (measured): 0 mm
 Wavelength: 546.07 nm
 Part Diameter: 0 mm

Select Results
 SAG IRR RSI RMT RMSi RMSa

Surface Type: Plane

Removed: PST TLT PWR Speichert bearbeitete Daten
 Apert OD (Fix): *** mm Apert ID (Fix): 0 mm
 Filter: Low Pass Trimmed: 0

Z490 Surface/Wavefront Profile

Removed: PST TLT PWR Speichert bearbeitete Daten
 Apert OD (Fix): *** mm Apert ID (Fix): 0 mm
 Filter: Low Pass Trimmed: 0

Auto Aperture: On
 Apert OD (Fix): 35.00 mm
 Apert ID (Fix): 0 mm
 Trim: 0
 Trim Mode: Outside
 Aperture Dimension(s): Fixed

Remove Filter: Low Pass
 PST TLT PWR AST CMA SA3 Filter Type: Average
 Filter Tr Filter Tr Filter Tr
 Filter Wi Filter Wi Filter Wi

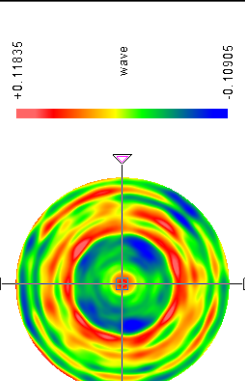
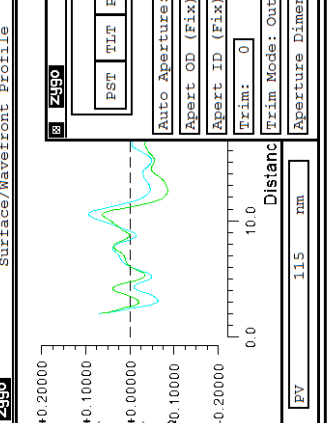
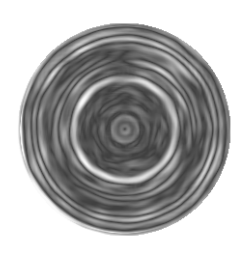
Height (ave) Distance
 +0.20000 0.0 10.0 115 mm
 +0.10000
 +0.00000
 -0.10000
 -0.20000

Z490 Measurement Attributes

Analysis Attributes
 Data Sign: Normal
 Scale Factor: 0.5
 Camera Res: 39.6 µm

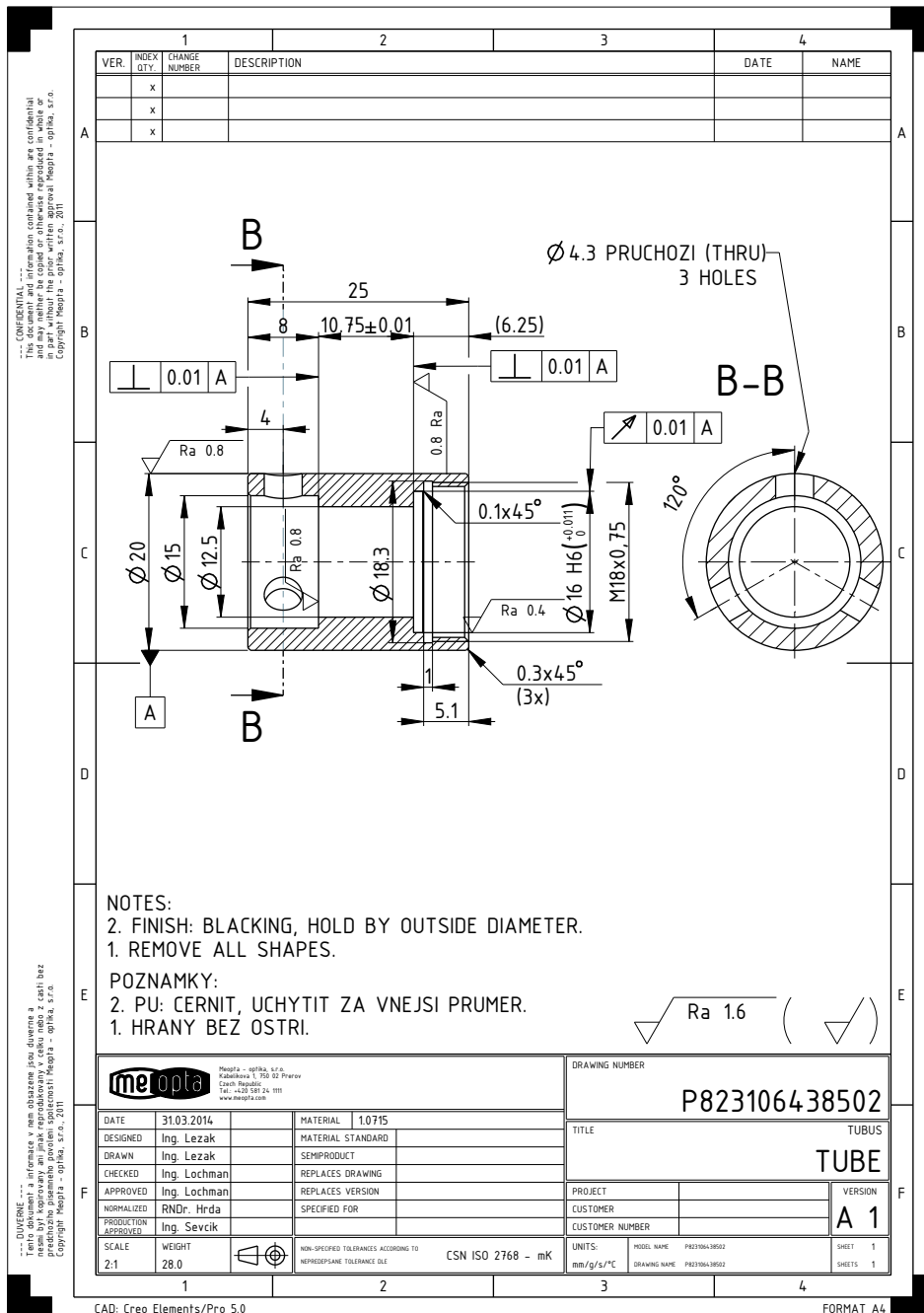
Report
 S/N: 76
 Units

Peak 0.50 min

Appendix D

LENS 6: Mechanics for Null Compensator



Bibliography

- [1] Goran Bastian Baer, Johannes Schindler, Christof Pruss, and Wolfgang Osten. Measurement of aspheres and free-form surfaces with the tilted-wave-interferometer. In Wolfgang Osten, editor, *Fringe 2013*, pages 87–95. Springer Berlin Heidelberg, 2014. ISBN 978-3-642-36358-0.
- [2] Volkmar Fischer and Takashi Matsuura. Optics manufacturing: Pressing makes precision aspheres faster and cheaper. *Laser Focus World*, 5(31):167, 1995.
- [3] M. Bass and Optical Society of America. *Handbook of Optics: Fundamentals, techniques, and design*. Number vol. 1 in Handbook of Optics. McGraw-Hill, 2nd edition, 1995. ISBN 9780070477407.
- [4] W.I. Kordonski and S.D. Jacobs. Magnetorheological finishing. *International Journal of Modern Physics B*, 10(23n24):2837–2848, 1996.
- [5] A.B. Shorey, D. Golini, and W. Kordonski. Surface finishing of complex optics. *Optics and Photonics News*, 18(10):14 – 16, 2007.
- [6] D. Malacara-Hernández, Z. Malacara-Hernández, and Z. Malacara. *Handbook of Optical Design, Second Edition*. Optical Science and Engineering. Taylor & Francis, 2003. ISBN 9780203912942.
- [7] C. Heij and C. Heij. *Econometric Methods with Applications in Business and Economics*. OUP Oxford, 2004. ISBN 9780199268016.
- [8] Daniel Malacara. *Optical Shop Testing*. Optical Shop Testing. John Wiley & Sons, Inc., 2nd edition, 2007. ISBN 9780470135969.
- [9] H. E. Dall. A null test for paraboloids. *Amateur Telescope Making*, 3:149–153, 1953.
- [10] David R. Shafer. Zoom null lens. *Appl. Opt.*, 18(22):3863–3865, Nov 1979.
- [11] Abe Offner. A null corrector for paraboloidal mirrors. *Applied Optics*, 2(2):153, 1963. ISSN 1559128X.
- [12] J. C. Wyant and V. P. Bennett. Using computer generated holograms to test aspheric wavefronts. *Appl. Opt.*, 11(12):2833–2839, Dec 1972.
- [13] Steven M. Arnold. How to test an asphere with a computer generated hologram, 1989.

- [14] S. Peterhänsel, C. Pruss, and W. Osten. Phase errors in high line density cgh used for aspheric testing: beyond scalar approximation. *Opt. Express*, 21(10):11638–11651, May 2013.
- [15] Jean-Michel Asfour and Alexander G. Poleshchuk. Asphere testing with a fizeau interferometer based on a combined computer-generated hologram. *J. Opt. Soc. Am. A*, 23(1):172–178, Jan 2006.
- [16] M.M. Talha, Jun Chang, Yongtian Wang, Dewen Cheng, Tingcheng Zhang, M. Aslam, and A. Naeem Khan. Computer generated hologram null compensator for optical metrology of a freeform surface. *Optik - International Journal for Light and Electron Optics*, 121(24):2262 – 2265, 2010. ISSN 0030-4026.
- [17] Stephan Reichelt, Christof Pruss, and Hans J. Tiziani. Specification and characterization of cghs for interferometrical optical testing, 2002.
- [18] Ping Zhou and James H. Burge. Optimal design of computer-generated holograms to minimize sensitivity to fabrication errors. *Opt. Express*, 15(23):15410–15417, Nov 2007.
- [19] Brian E. Catanzaro, James A. Thomas, and Eri J. Cohen. Comparison of full-aperture interferometry to subaperture stitched interferometry for a large-diameter fast mirror, 2001.
- [20] S. Zeng, Y. Dai, and S. Chen. Subaperture stitching interferometer for large optics. In *Society of Photo-Optical Instrumentation Engineers (SPIE) Conference Series*, volume 7281 of *Society of Photo-Optical Instrumentation Engineers (SPIE) Conference Series*, May 2009.
- [21] Xi Hou, Fan Wu, Shibin Wu, and Qiang Chen. Annular subaperture interferometric testing technique for large aspheric surfaces, 2005.
- [22] Xiaokun Wang, Lihui Wang, Longhai Yin, Binzhi Zhang, Di Fan, and Xuejun Zhang. Measurement of large aspheric surfaces by annular subaperture stitching interferometry. *Chin. Opt. Lett.*, 5(11):645–647, Nov 2007.
- [23] X.-K. Wang, L.-H. Wang, L.-G. Zheng, W.-J. Deng, and X.-J. Zhang. Annular sub-aperture stitching interferometry for testing of large aspherical surfaces. *Proceedings of SPIE - The International Society for Optical Engineering*, 6624, 2008.
- [24] Andrew Kulawiec. Extended aspheric measurement capability with subaperture stitching interferometry. *EuroPhotonics*, 13(5):32–33, 2008.
- [25] Shanyong Chen, Yifan Dai, Shengyi Li, and Xiaoqiang Peng. Calculation of subaperture aspheric departure in lattice design for subaperture stitching interferometry. *Optical Engineering*, 49(2):023601–023601–5, 2010.
- [26] Paul Murphy, Gary DeVries, Jon Fleig, Gregory Forbes, Andrew Kulawiec, and Dragisha Miladinovic. Measurement of high-departure aspheric surfaces using subaperture stitching with variable null optics, 2009.

- [27] M. Tricard, A. Kulawiec, M. Bauer, G. DeVries, J. Fleig, G. Forbes, D. Miladinovich, and P. Murphy. Subaperture stitching interferometry of high-departure aspheres by incorporating a variable optical null. *CIRP Annals - Manufacturing Technology*, 59(1):547–550, 2010.
- [28] Ricarda Kafka and Thomas Blümel. Interferometric testing of aspheres based on programmable eghs. *International Photonics Cluster Summer School in Adaptive Optics and Microoptics*, August 2006.
- [29] 2014. URL <http://www.nuffieldfoundation.org/practical-physics/application-newtons-rings-experiment>.
- [30] Daniel Malacara, M. Servín, and Z. Malacara. *Interferogram Analysis for Optical Testing*. Optical Science and Engineering. Taylor & Francis, 1998. ISBN 9780824799403.
- [31] M. Mansuripur. *Classical Optics and Its Applications*. Cambridge University Press, 2002. ISBN 9780521804998.
- [32] *ESDI Intellium Sub-Nyquist Interferometry Overview*, 2012.
- [33] B. Dörband, H. Gross, and H. Müller. *Handbook of Optical Systems, Metrology of Optical Components and Systems*. Gross/Optical Systems V1-V6 special prices until 6V ST published. Wiley, 2012. ISBN 9783527403813.
- [34] J. Pfund, N. Lindlein, and J. Schwider. Dynamic range expansion of a shack–hartmann sensor by use of a modified unwrapping algorithm. *Opt. Lett.*, 23(13):995–997, Jul 1998.
- [35] Sascha Groening, Bernhard Sick, Klaus Donner, Johannes Pfund, Norbert Lindlein, and Johannes Schwider. Wave-front reconstruction with a shack-hartmann sensor with an iterative spline fitting method. *Appl. Opt.*, 39(4):561–567, Feb 2000.
- [36] Andrew E. Lowman and John E. Greivenkamp. Modeling an interferometer for non-null testing of aspheres. *Proc. SPIE*, 2536:139–147, 1995.
- [37] *Intellium Z100 manual*, 2012.
- [38] Michael F. Küchel. Interferometric measurement of rotationally symmetric aspheric surfaces, 2009.
- [39] *Intelliwave 6.5 software manual*. ESDI, 2009.
- [40] Dong Liu, Yongying Yang, Chao Tian, Yongjie Luo, and Lin Wang. Practical methods for retrace error correction in nonnull aspheric testing. *Opt. Express*, 17(9):7025–7035, Apr 2009.
- [41] Joseph M. Geary, K. M. Yoo, and Guojun Si. Retrace error: a case study. *Proc. SPIE*, 1776: 98–105, 1992.

- [42] Cody B. Kreischer. Retrace error: interferometry's dark little secret. *Proc. SPIE*, 8884:88840X–88840X–12, 2013.
- [43] Hongzhang Ma. Tolerancing optical systems, 2013. Study notes for Introductory Opto-Mechanical Engineering class, The University of Arizona.
- [44] 2014. URL http://www.saarstahl.com/fileadmin/saarstahl_extranet/images/04_produkte/walzstahlsorten/english/0715_11SMn30_9SMn28.pdf.
- [45] J. Porter, H. Queener, J. Lin, K. Thorn, and A.A.S. Awwal. *Adaptive Optics for Vision Science: Principles, Practices, Design and Applications*. Wiley Series in Microwave and Optical Engineering. Wiley, 2006. ISBN 9780471914648.